Simultaneous Improvements in Performance and Durability of an Octahedral PtNix/C Electrocatalyst for Next-Generation Fuel Cells by Continuous, Compressive, and Concave Pt Skin Layers

doi: 10.1021/acscatal.7b00964

Simultaneous Improvements of Performance and Durability of An Octahedral $PtNi_x$/C Electrocatalyst for Next–Generation Fuel Cells by Continuous, Compressive and Concave Pt skin layers

Xiao Zhao,[†] Shinobu Takao [†] Kotaro Higashi,[†] Takuma Kaneko,[†] Gabor Samjeskè,[†] Oki Sekizawa,[†] Tomohiro Sakata,[†] Yusuke Yoshida,[†] Tomoya Uruga[†,‡] and Yasuhiro Iwasawa[†]*

[†] Innovation Research Center for Fuel Cells, The University of Electro-Communications, Chofugaoka, Chofu, Tokyo 182-8585, Japan

[‡]Japan Synchrotron Radiation Research Institute, SPring-8, Sayo, Hyogo 679-5198, Japan

*Corresponding author: iwasawa@pc.uec.ac.jp

ABSTRACT. Simultaneous improvements of oxygen reduction reaction (ORR) activity and long-term durability of Pt-based cathode catalysts are indispensable for the development of next-generation polymer electrolyte fuel cells but are still a major dilemma. We present a robust octahedral core-shell $PtNi_x$/C electrocatalyst with high ORR performance (mass activity and surface specific activity: 6.8-16.9 and 20.3-24.0 times larger than Pt/C, respectively) and durability (negligible loss after 10,000 accelerated durability test (ADT) cycles). The key issues of the robust octahedral nanostructure (core-shell $Pt_{73}Ni_{27}$/C) responsible for the remarkable activity and durability were addressed to be continuous three Pt skin layers with 2.0-3.6% compressive strain, concave facet arrangements (concave defects and high coordination), a symmetric Pt/Ni distribution and a $Pt_{67}Ni_{33}$ intermetallic core by STEM-EDS, *in situ* XAFS, XPS, etc. The robust core-shell $Pt_{73}Ni_{27}$/C was produced by the partial release of the stress, Pt/Ni rearrangement and dimension reduction of an as-synthesized octahedral $Pt_{50}Ni_{50}$/C with 3.6-6.7% compressive Pt skin layers by Ni leaching during the activation process. The present results on the tailored synthesis of the $PtNi_x$ structure and composition and the better control of the robust catalytic architecture renew the current knowledge and viewpoint for instability of octahedral $PtNi_x$/C samples to provide a new insight into development of next-generation PEFC cathode catalysts.

Keywords: Robust octahedral core-shell $PtNi_x$/C electrocatalyst, Polymer electrolyte fuel cell, High performance and durability, Continuous, compressive and concave Pt skin layers, Structural and electronic property, *In situ* XAFS/STEM-EDS/XPS/ICP-AES.

INTRODUCTION

Remarkable improvements of both the oxygen reduction reaction (ORR) performance and long-term durability of the current Pt-based cathode catalysts under the harsh PEFC conditions are needed for wide-spread commercialization.[1-17] Although various electrocatalysts involving Pt-skin nanoparticles have been proposed as promising PEFC cathode catalysts,[15,18-24] carbon-supported Pt and Pt-bimetal catalysts are still considered to be the most active cathode catalysts for PEFCs, depending on a variety of key issues, such as nanoparticle size and shape (plane), surface roughness, compressive strain (bond distance), downward Pt d-band center, electronic modification (ligand effect), Pt-O bond strength, particle proximity, etc.[15,25-35] In contrast, key issues for simultaneous improvements of oxygen reduction reaction (ORR) performance and long-term durability of Pt-based electrocatalysts under potential-operation conditions in acidic media are hard to be adequately addressed yet, which prevents developing new durable cathode catalysts toward next-generation PEFCs.

Recently, several Pt-based cathode catalysts with remarkable performances have been reported; e.g. nano-structured Pt/C, Pt-additive metal/C, etc. as typically listed in Table 1.[25,35-42] However, most of them show insufficient durability except for specific samples, such as nanoframe Pt_3Ni/C (Pt_3Ni further coated with the thermally segregated Pt skin),[41] Mo-Pt_3Ni/C (Pt_3Ni further doped with Mo),[37] jagged nanowire Pt/C (fabricated from Pt@NiO with H_2),[25] and Pt@PtPb/C (thin-nanoplate core-shell)[43] at rotating disk electrodes (RDE). While the structured electrocatalysts have been reported as promising candidates, alternative approaches towards highly active and stable catalysts preferably with low Pt are requested. DFT calculations on unique Pt-lanthanide/C prepared by a sputtering method showed that the stability decreases as the compressive strain increases,[35] while reversely the ORR activity increases with increasing strain. The DFT calculations also suggested that Pt_5Tb/C, most active among the examined Pt-lanthanide/C, should exhibit ~3% compression,[35] though the durability is insufficient as shown in Table 1. A $Pt_3Ni(111)$ crystal surface is regarded to be the most active surface so far.[4] Among practical Pt-based bimetal electrocatalysts octahedral $PtNi_x$/C with {111} facets also showed remarkable mass activities (MAs) of 1.65-3.3 A mg^{-1}_{Pt} at 0.9 V_{RHE} (vs. RHE) and surface specific activities (SAs) of 3.8-10.6 mA cm^{-2}_{Pt} at 0.9 V_{RHE}.[44] However, rapid deactivation occurs with those octahedral electrocatalysts and the

MAs decrease by 40-66% after 5000 accelerated durability test (ADT) cycles at around 0.6-1.0 V_{RHE} (Table 1).[37,38,40,45,46] The trend-off aspect may be in a dilemma. In Pt-bimetal systems the preferential and ready dissolution of non-Pt components occurs under changing potentials in acidic media. Thus, most bimetal systems may not be stable due to leaching and segregation over time.[47] At the moment our understanding of structural behaviors of cathode nanoparticle surfaces governing the long-term durability of cathode catalysts under the PEFC conditions is still incomplete. Tailored synthesis of the structure and composition that can improve/optimize durability/performance in Pt-alloys is mandatory.

Table 1. Electrochemical surface areas, activities and durabilities of recent Pt-based cathode catalysts with remarkable ORR activities including Pt/C as reference for comparison with our work

Catalyst	ECSA	MA @0.9 V (@0.95 V) (A mg^{-1}_{Pt})	SA @0.9 V (@0.95 V) (mA cm^{-2}_{Pt})	Durability/Loss	Ref.
TEC10E20E	96.0	0.25 (0.033)	0.26 (0.035)	10000 cycles, 0.6-1.0 V, **32% MA loss**	This work
TEC10E50E	--	--	0.25*	10000cycles, 0.6-1.0 V, **31% MA loss****	*37,**This work
TEC10E50E-HT	45.0	0.10	0.22	10000cycles, 0.6-1.0 V, **25% MA loss**	This work
Pt_3Ni/C dendrites	37.1	0.75 (0.086)	2.03 (0.23)	--	This work
$Pt_{73}Ni_{27}$/C octahedral	32	1.69 (0.29)	5.29 (0.90)	10000 cycles, 0.6-1.0 V, **3.7% MA loss**	This work
Pt_5Tb/C	--	--	11.2	10000 cycles, 0.6-1.0 V, **33% SA loss**	35
Pt@PtPb /C nanoplate	55.0	4.3	7.8	50000 cycles, 0.6-1.1 V, **7.7% MA loss**	43
Pt_3Ni/C nanoframe	50.4	(0.43)	(0.86)	--	39
$Pt_{2.4}Ni$/C octahedral	46.4	2.67	5.74	10000 cycles, 0.6-1.1 V, **60% MA loss**	40
Pt/C jagged nanowire	118	13.6	11.5	6000 cycles, 0.6-1.0 V, **12% MA loss**	25
Pt/C octahedral nanocage	38.2	0.75	1.98	10000 cycles, 0.6-1.1 V, **36% MA loss**	38
Pt_3Ni/C octahedral	81.9	1.8 (0.37)	2.2 (0.45)	8000 cycles, 0.6-1.1 V, **59% MA loss**	37
Mo-Pt_3Ni/C octahedral	83.9	6.98 (1.41)	8.2 (1.74)	8000 cycles, 0.6-1.1 V, **5.5% MA loss**	37
Pt@Ni/C-Pt skin octahedral skeletal	28	1.12	4.0	--	36
Pt_3Ni/C nanoframe-Pt skin	65.5	5.7 (0.97)	8.7 (1.48)	10000 cycles, 0.6-1.0 V, **negligible loss**	41
Pt_xY/C	22.8	3.05	13.4	9,000 cycles, 0.6-1.0 V, **37% MA loss**	42
$Pt_{2.5}Ni$/C octahedral	31	3.3	10.6	5000 cycles, 0.65-1.0 V, **40% MA loss**	46
PtNi/C octahedral	48	1.65	3.8	4000 cycles, 0.6-1.0 V, **66% MA loss**	45
Pt_3Ni(111)- Pt skin	--	--	18	--	4
Pt(111)	--	--	1.8	--	4

Here, we report a robust octahedral core-shell $Pt_{73}Ni_{27}$/C electrocatalyst with high ORR performance and durability, which can be facilely fabricated by a synthesis procedure and an electrochemical activation process without further deposition of Pt skin layers and H_2 thermal reduction. The as-synthesized, activated and ADT (10,000 cycles) $PtNi_x$/C electrocatalysts were characterized by TEM/STEM-EDS, *in situ* Pt L_3-edge and Ni K-edge XAFS, Pt 4f and Ni 2p XPS, etc. The present work may renew the current knowledge and viewpoint for instability of octahedral $PtNi_x$/C samples.

EXPERIMENTAL SECTION

Preparation of octahedral and dendrite Pt-Ni/C electrocatalysts. Platinum(II) acetylacetonate ($Pt(acac)_2$), nickel(II) acetylacetonate ($Ni(acac)_2$), polyvinyl pyrrolidone (PVP), methyl formate (MF) and N, N-dimethylformamide (DMF), perchloric Acid (TraceSELECT®) were all purchased from Sigma-Aldrich. All the chemicals were used as received without further purification. Ultra-pure water (18 MΩ·cm) purified in a Millipore system was used in all experiments.

Octahedral $PtNi_x$ nanocrystals were typically prepared as follows. $Pt(acac)_2$ (40 mg), ($Ni(acac)_2$ (26 mg), PVP (520 mg) and DMF (40 mL) were added into a vial. After the vial was capped, the solution was mixed for 1 h. Then, MF (0.4 mL) was added into the solution and the mixture was stirred for 5 min. Lastly, this solution was transferred into a Teflon-lined stainless steel autoclave (100 mL), which was heated at 130 ^oC for 12 h. After cooling, the product was collected by centrifugation and washed with ethanol/acetone (V/V=1:1) and Millipore water/ethanol (V/V=1:1) for several times. The obtained sample was then dispersed in a Millipore water/ethanol (V/V=1:1) solution.

Dendrite $PtNi_y$ nanocrystals were prepared by a similar procedure for the octahedral $PtNi_x$ nanocrystals without utilization of MF.

Carbon supported octahedral $PtNi_x$ and dendrite Pt_3Ni nanocrystals were prepared by using carbon black (Vulcan XC-72) as follows. Vulcan XC-72 was well-dispersed in a Millipore water/ethanol (V/V=1:1) solution, to which the octahedral $PtNi_x$ and dendrite $PtNi_y$ nanocrystals fabricated above were poured, then dispersed under stirring and ultrasonic condition overnight. Finally, the dispersion was filtered and washed with ethanol and a large amount of Millipore water, followed by drying at 40^oC under vacuum. The Pt loadings in the octahedral and dendrite $PtNi_x$/C were regulated as 20 wt%. Commercial Pt/C electrocatalysts (TEC10E20E and TEC10E50E-HT) were purchased from Tanaka Kikinzoku Kogyo and used as references for comparison.

Electrochemical Measurements. All glassware for electrochemical measurement was treated by qua regia, and boiled water, and then washed by Millipore water thoroughly. A 0.1 M $HClO_4$ solution was prepared using perchloric Acid (TraceSELECT®, Sigma-Aldrich) and 18.2 MΩ·cm Millipore water. The electrocatalyst ink formulation is 1 mg electrocatalyst/0.5 mL Millipore water /0.4 mL isopropanol/0.005 ml 5 wt% Nafion®. The testing temperature is room temperature. Pt foil and RHE were used as counter and reference electrodes, respectively. Electrocatalyst thin-film working electrode with a Pt loading of 12 μg_{Pt} cm^{-2}_{geo} was prepared by a spin coating method on a 5 mm rotating disk electrode (RDE). Electrochemical performances presented in this study are values based on at-least five independent measurements.

The electrochemical measurements were conducted by the following procedures.

Activating processes: The working electrodes were potentially cycled from 0.02 to 1.2 V_{RHE} at a scan rate of 100 mV s^{-1} in N_2-saturated 0.1 M $HClO_4$ until a stable response was obtained; typically 50 cycles.

Electrochemical surface areas ($ESCA_{Hupd}$): They were estimated from the integration of under-potentially deposited hydrogen. The working electrodes were cycled three times between 0.025 and1.2 V_{RHE} at a scan rate of 50 mV s^{-1} in N_2-saturated 0.1 M $HClO_4$. The third cyclic voltammograms (CV) was used for calculation of the $ESCA_{Hupd}$.

Electrocatalytic performances: They were estimated by linear sweep voltammetry (LSV) from 0.0 to 1.05 V at a scan rate of 20 mV s^{-1} in O_2-saturated 0.1 M $HClO_4$ at 1600 rpm. The measurements were repeated three times and a maximum current at 0.9 V_{RHE} among them was used for the activity calculation.

R_{sol}: The i-interrupter method was used for the measurement of solution resistance R_{sol}, which was used for IR-compensation.

CO stripping tests: Firstly, the CO adsorption was conducted through chronoamperometry with a stepped potential to 0.4 V_{RHE} in CO-saturated 0.1 M $HClO_4$ for 5 min, followed by removal of residual CO in 0.1 M $HClO_4$ by bubbling N_2 for 30 min. Secondly, the working electrode with pre-adsorbed CO was potentially cycled two times from 0.025 to 1.2 V_{RHE} at a scan rate of 50 mV s^{-1}, where the second cycle was used for checking if pre-adsorbed CO was removed completely. The CO stripping voltammograms were used for calculation of electrochemical surface areas ($ESCA_{CO}$).

Accelerated durability test (ADT): The ADT was conducted by square-wave potential cycles of 3 s at each 0.6 and 1.0 V_{RHE} up to 10000 cycles in O_2-saturated 0.1 M $HClO_4$ according to an ADT protocol of the Fuel Cell Commercialization Conference of Japan (FCCJ), which has widely been studied.

$ESCA_{Hupd}$ and electrocatalytic activity after ADT: The working electrode was washed by Millipore water, and then subsequent electrochemistry measurements were conducted in a fresh 0.1 M $HClO_4$ solution by a procedure similar to the one mentioned above.

The electrochemical performances of initial/as-prepared electrocatalysts without the activating process were also evaluated similarly. It is notable that these evaluation processes will cause a change in the structure of the electrocatalysts to some extent. Thus, the initial /as-prepared activity does not reflect the real as-prepared state. Fortunately, it does not affect the judgment of the trend in structure and electroactivity during the activating and ADT processes.

***In situ* X-ray absorption fine structure (XAFS).**[48] Potential-dependent *in situ* XAFS spectra at Pt L_{III}-edge and Ni K-edge for the activated $PtNi_x$/C and Pt/C electrocatalysts at rotating disk electrodes (RDE) in N_2-saturated 0.1 M $HClO_4$ at 1600 rpm were measured in a fluorescence mode by using a Si(111) double-crystal monochromator and an ion chamber (I_0: Ar 5% / N_2 95%) for incident X-rays and a 21 Ge-elements detector for fluorescent X-rays at BL36XU station in SPring-8. The BL36XU beamline with several XAFS systems for characterization of fuel cells was constructed by our group under a NEDO program.[48,49] The XAFS measurements and analysis were performed similarly to the previous reports.[15,50-52]

X-ray absorption near-edge structure (XANES) spectra were normalized by Athena software.[53] The XAFS spectra were treated with the data analysis program IFEFFIT (version 1.2.11c).[54] Theoretical phase shifts and amplitude functions for Pt-Pt, Pt-Ni and Pt-O were calculated from FEFF 8.20.[55] The extracted EXAFS oscillations were k^2-weighted and Fourier transformed to r-space and the curve fittings of k^2-weighted EXAFS data in R-space were carried out with Artemis.[53] Fitting parameters for each shell were coordination number (CN), interatomic distance (R), Debye-Waller factor (σ^2), and correction-of-edge energy (ΔE_0).[15,50-52] Error ranges of the curve-fitting analysis of EXAFS Fourier transforms were based on the definition of the IFEFFIT code in the Artemis program.[53]

Transmission electron microscope (TEM) and scanning TEM (STEM)/ energy-dispersive X-ray spectroscopic (EDS) images. *Ex situ* TEM and STEM-EDS images were measured on a JEM-2100F equipped with an energy dispersive spectrometer (EDS) at 200 kV. TEM and STEM samples were prepared by dispersing electrocatalysts in ethanol by sonication, putting the dispersed electrocatalysts on carbon film deposited on Cu grids, and drying.[15,56]

X-ray photoelectron spectra (XPS) measurements. Pt 4f and Ni 2p XPS spectra were measured by JEOL JPS-9200 using Mg Kα radiation at 10 kV and 10 mA as an excitation source. The XPS binding energies were referred to that of C 1s in a graphitic state (284.5 eV). XPS spectra were measured as follows. The electrocatalyst ink was dropped on a glass carbon plate, followed by drying at room temperature, which was used as a working electrode. The obtained working electrodes were treated by an electrochemical activating process and washed by N_2 saturated--deionized water. The working electrodes covered with N_2-saturated deionized water were immediately transferred into a preparation chamber for the Pt 4f and Ni 2p XPS measurements.

XRD measurements. The powder electrocatalysts were characterized by X-ray diffraction (XRD, Rigaku RINT2000) with Cu Kα radiation generated at 40 kV and 40 mA in the 2θ range of 10−90^o at a step scan speed of 0.02^o s^{-1}. In the case of the activated samples, the samples after XPS measurements were subsequently used for XRD measurements.

Bulk composition analysis. The bulk compositions of Pt and Ni atoms in the as-prepared $PtNi_x$ nanoparticles (before supporting) and the as-synthesized, activated, and ADT $PtNi_x$/C electrocatalysts were estimated by an inductively coupled plasma atomic emission spectroscopy (ICP-AES, Shimadzu ICPS-8100) and X-ray fluorescence (XRF, Rigaku ZSX Primus2). "A given amount of samples in quartz beakers was first heated at 800℃ in air. Then, the residual samples were dissolved in nitric acid hydrochloride (1:1) and diluted to 50 mL solution by pure water." Quantifications of Pt and Ni were carried out by making their standard curves. The bulk compositions of the as-synthesized, activated, and ADT $PtNi_x$/C electrocatalysts were also estimated by measuring several nanoparticles with EDS equipped on STEM.

RESULTS AND DISCUSSION

1. Fabrication and electrocatalytic activity and durability of a robust octahedral $PtNi_x$/C. To fabricate octahedral $PtNi_x$/C electrocatalysts with both high ORR activity and robust durability we used metal precursors, $Pt(acac)_2$ and $Ni(acac)_2$ with a 1:1 ratio in DMF solvent. They were reduced to $PtNi_x$ alloy nanoparticles by methyl formate (MF) as a reducing agent in the presence of polyvinyl pyrrolidone (PVP) as a capping agent at 130^{o}C for 12 h, followed by centrifugation and deposition on carbon black

(Vulcan XC-72). The as-synthesized $PtNi_x$/C samples were activated by CV cycles between 0.025－1.2 V_{RHE} at a scan rate of 100 $mV \cdot s^{-1}$ in N_2-saturated 0.1 M $HClO_4$. The synthesis methods for the previous octahedral $PtNi_x$/C electrocatalysts are described in Supporting Information (SI) for comparison with our synthesis method.[36,37,45,46]

Figure 1 shows TEM images of typical $PtNi_x$ nanoparticles with different structures and shapes synthesized by using different amounts of MF in the presence (a-d) and absence (e and f) of PVP at 130°C (more in Figure S1, where other $PtNi_x$ nanoparticles fabricated in different conditions are shown). Under the synthesis conditions without PVP $PtNi_x$ nanoparticles aggregated in an uncontrollable manner. In the presence of PVP the amount of MF was a key parameter for the synthesis of featured $PtNi_x$ nanoparticles. At 0 mL of MF Pt_3Ni dendrites were produced as shown in Figure 1 (a), and by increasing the MF quantity each particle grew, and at 0.4 mL of MF octahedral $Pt_{50}Ni_{50}$ nanoparticles with an averaged particle size of 14.2 ± 1.9 nm were fabricated as shown in Figure 1 (c) and Figure S1. Further increase of the MF quantity grew particles to sizes above 20 nm and to form grained nanostructured $PtNi_x$ particles (Figure 1 (d)). Thus the MF reducing agent can tune the nanostructured feature. The MF amount, the ratio of MF/PVP and fabrication temperature and period totally affected the shape and size of as-synthesized octahedral $PtNi_x$ nanoparticles. We examined the electrochemical property of the two representative

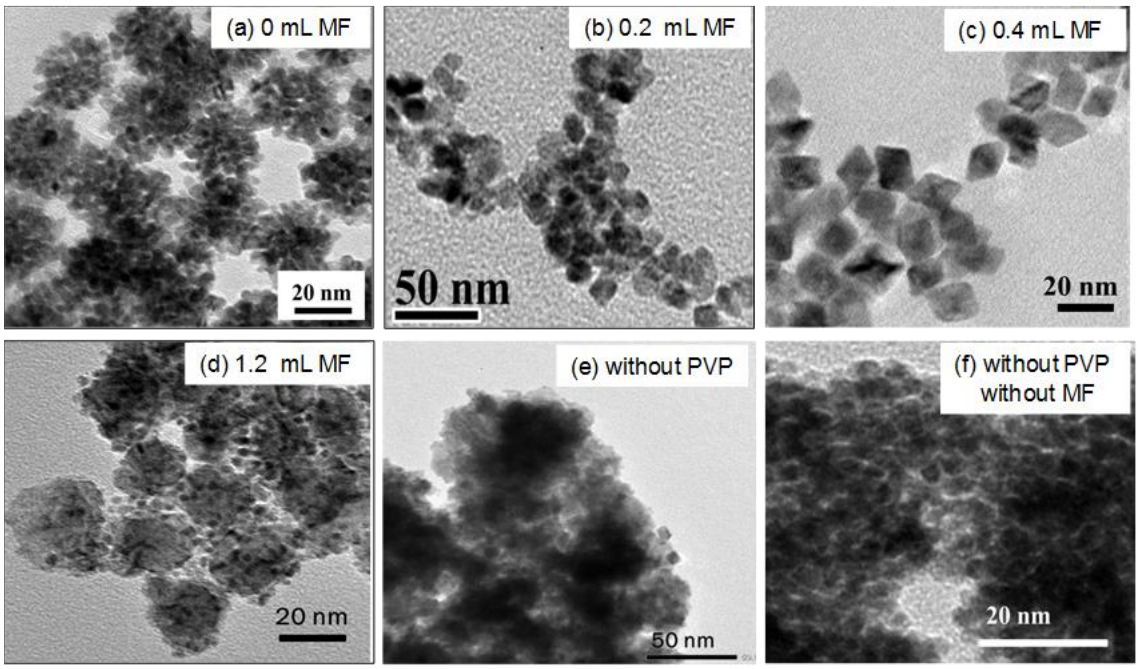

Figure 1. TEM images of various as-synthesized $PtNi_x$ nanoparticles obtained by changing the MF quantity with and without PVP. (a): PVP, (b)-(d): PVP+MF, (e): MF, (f): neither PVP nor MF.

samples, the nanodendrites and octahedral nanoparticles as shown in Figure 1 (a) and (c), respectively because the two samples have relatively homogeneous shapes and sizes among the obtained nanoparticles. The Pt/Ni compositions were determined by XRF, EDS and ICP-AES.

Figure 2 (a) and (b) show the CV and CO stripping curve for the activated octahedral $Pt_{73}Ni_{27}$/C and the CO stripping curves for the activated Pt/C, dendrite Pt_3Ni/C and octahedral $Pt_{73}Ni_{27}$/C, respectively. The electrochemical surface areas (ECSAs) were estimated by integrated charge from CO_{ad} and H_{upd}. The

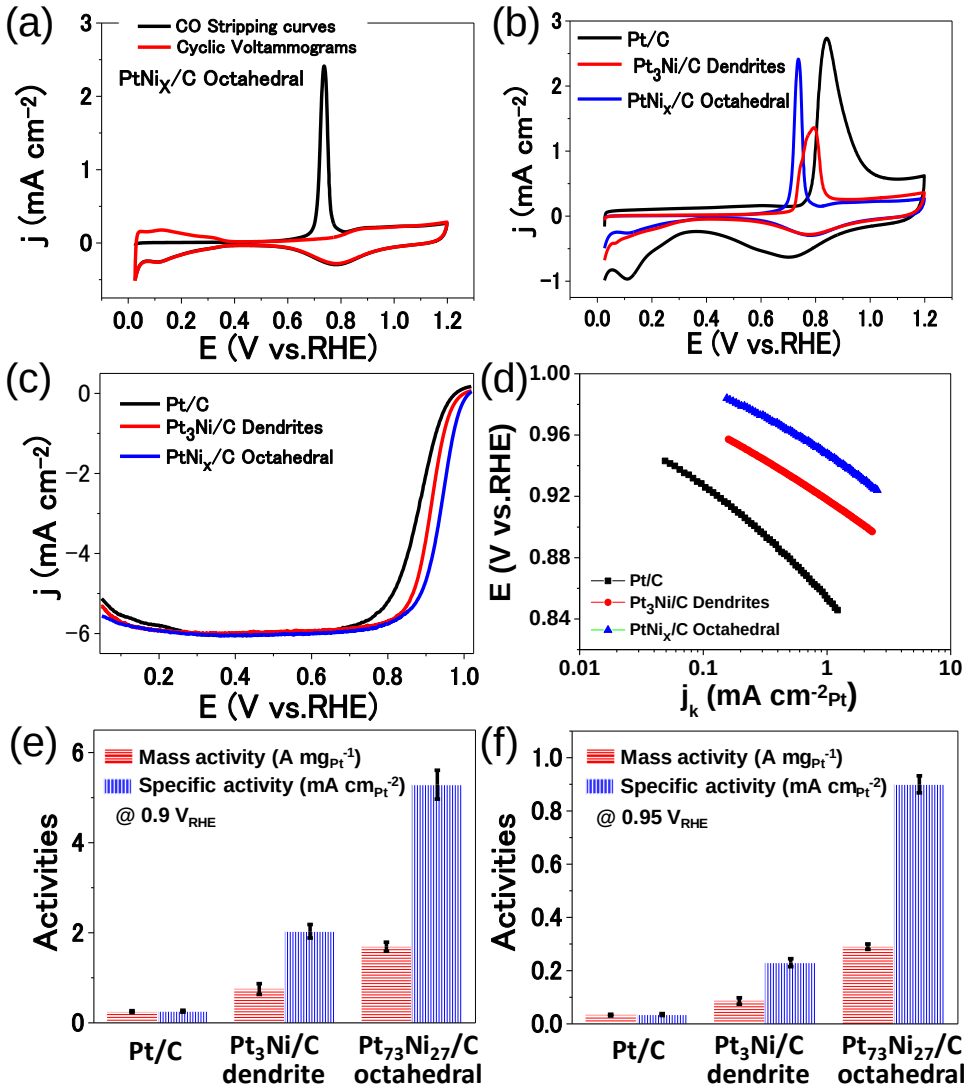

Figure 2. Electrochemical properties of the activated electrocatalysts, Pt/C (TEC10E20E), dendrite Pt_3Ni/C and octahedral $Pt_{73}Ni_{27}$/C($PtNi_x$/C). (a) CO stripping curve and cyclic voltammogram for the octahedral $PtNi_x$/C. (b) CO stripping curves for the octahedral $PtNi_x$/C, dendrite Pt_3Ni/C and Pt/C. (c) ORR polarization curves; (d) the corresponding Tafel plots; (e) and (f) the mass and specific activities at 0.9 V_{RHE} (e) and 0.95 V_{RHE} (f), respectively calculated by the Koutecky-Levich equation.

ratio between $ECSA_{CO}$ and $ECSA_H$ values for the octahedral $Pt_{73}Ni_{27}/C$ was 0.99 (Figure 2 (a)). It has been demonstrated that when $PtNi_x/C$ core-shell samples possess a Pt monolayer skin and a Ni-enriched second layer, the ratio $ECSA_{CO}/ECSA_H$ is 1.5, while $PtNi_x/C$ samples without monolayer Pt-skin structure and Pt/C samples show the ratio of 1.0.[57] Hence, our octahedral $Pt_{73}Ni_{27}/C$ may possess more than two Pt layers at the surface. The more positive potential for oxygen electro-adsorption/desorption (the weaker strength of oxygen adsorption) on $PtNi_x/C$ than on Pt/C in the cyclic voltammograms (O_2 desorbs at 0.78 V_{RHE} for $PtNi_x/C$ and 0.70 V_{RHE} for Pt/C) as shown in Figure 2 and Figure S2. The relative strength of oxygen adsorption/desorption is consistent with the activity trend for $PtNi_x/C$ and Pt/C. However, if we turned to the octahedral and dendrite $PtNi_x/C$ catalysts, the two catalysts have much different activities from each other, but they showed the similar potentials for oxygen adsorption/desorption in the cyclic voltammogram. This inconsistence may be due to the different structures between the octahedral and dendrite $PtNi_x/C$. The CO stripping reaction is known to be structure-sensitive, which may show a better consistent trend with the ORR activity for the current catalysts. The CO stripping peak for the octahedral $Pt_{73}Ni_{27}/C$ (0.74 V_{RHE}) shifted by 100 mV to the lower potential compared to that for the Pt/C reference (0.84 V_{RHE}) in Figure 2 (b). The shift of the CO stripping peak for the dendrite Pt_3Ni/C (0.79 V_{RHE}) was 60 mV. These down shifts are larger than the shifts for the previously reported Pt_3Ni alloy/C (11 mV) and Pt_3Co alloy/C (22 mV), which are Pt-alloy electrocatalysts in a highest activity level among Pt_3M/C series (M: transition metals).[13,15] It is reported that the higher Pt d-band center energy induces the stronger CO adsorption due to a decrease in the electron back-donation from Pt to the antibonding orbitals of CO molecules and the CO stripping potentials at Pt and Pt-alloy nanoparticle surfaces have been correlated directly with Pt d-band center.[15,58-61] Thus, it is suggested that the surfaces of the dendrite Pt_3Ni/C and particularly, octahedral $Pt_{73}Ni_{27}/C$ have the weaker oxygen adsorption strength than the Pt_3Ni/C .

The ORR activities of the dendrite Pt_3Ni/C and octahedral $Pt_{73}Ni_{27}/C$ electrocatalysts were evaluated by the polarization curves in O_2-saturated 0.1 M $HClO_4$ solution (Figure 2 (c)). The MA and SA increased in the order, Pt/C (TEC10E20E) < dendrite Pt_3Ni/C < octahedral $Pt_{73}Ni_{27}/C$ as shown in Figure 2 (e) (@0.9 V_{RHE}) and (f) (@0.95 V_{RHE}), where the three electrocatalysts have the similar Pt loadings (20 wt%). The MA and SA values are listed in Table 1. The kinetic current densities were calculated by the Koutecky-Levich equation and used for the Tafel plot (Figure 2 (d)). With a Tafel slope of 49 mV dec^{-1}, the octahedral $Pt_{73}Ni_{27}/C$ showed a much higher activity than Pt/C with 76 mV dec^{-1}. It is notable that the MA and SA of the octahedral $Pt_{73}Ni_{27}/C$ with an average particle size of 14.0 nm exhibited much higher values, 6.8 times and 20.3 times, respectively than those of commercial Pt/C (TEC10E20E) with an

average particle size of 2.3 nm (Figure 2 (e) and Table 1). The octahedral $Pt_{73}Ni_{27}$/C was also much more active than a commercial Pt/C (TEC10E50E- HT) with 50.9 wt% Pt loading and an average Pt particle size of 5.1 nm, which is relatively closer to the particle size of the $Pt_{73}Ni_{27}$/C, showing the MA and SA16.9 and 24.0 times higher, respectively (Table 1).

The most striking feature of the octahedral $Pt_{73}Ni_{27}$/C is high durability. The loss of the MA of the octahedral $Pt_{73}Ni_{27}$/C after 10,000 ADT cycles was as small as 3.7% as shown in Figure 3 (a) and (b). The ECSA also only reduced by 4.4% after 10,000 ADT cycles. In contrast, previous octahedral $PtNi_x$/C electrocatalysts showed insufficient durability (40-66% MA loss), while exhibiting high activities[37,40,45,46] as shown in Figure 2 (e) at 0.9 V_{RHE} and (f) at 0.95 V_{RHE} and Table 1. Typically, the octahedral $Pt_{2.4}Ni$/C and $Pt_{2.5}Ni$/C prepared by the reduction of $Pt(acac)_2$ and $Ni(acac)_2$ with $W(CO)_6$ in the presence of oleylamine and oleic acid exhibited 60% MA loss after 10,000 ADT cycles and 40% MA loss after 5,000 ADT cycles.[40,46] the octahedral Pt_3Ni/C prepared by heating of $Pt(acac)_2$, $Ni(acac)_2$ and benzoic acid in DMF exhibited 59% MA loss after 8,000 ADT cycles,[37] and the octahedral PtNi/C prepared by heating of $Pt(acac)_2$ and $Ni(acac)_2$ in DMF exhibited 66% MA loss after 4,000 ADT cycles.[45] It is difficult to

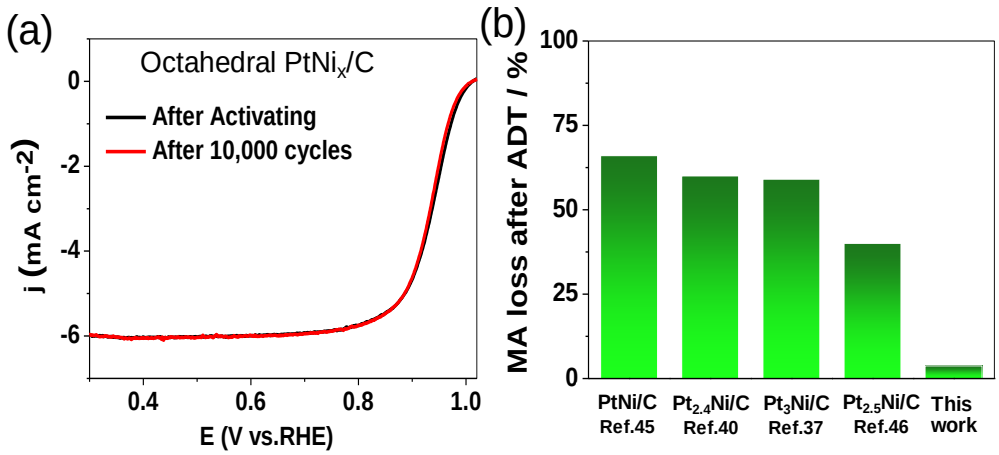

Figure 3. Electrochemical properties of the activated electrocatalysts, Pt/C (TEC10E20E), dendrite Pt_3Ni/C and octahedral $Pt_{73}Ni_{27}$/C($PtNi_x$/C). (a) ORR polarization curves of the octahedral $Pt_{73}Ni_{27}$/C($PtNi_x$/C) after aging and ADT 10,000 cycles. (b) Comparison of the durability (MA loss % after the ADT 10,000 cycles) among the octahedral Pt-Ni/C catalysts, PtNi/C, $Pt_{2.4}Ni$/C, Pt_3Ni/C, $Pt_{2.5}Ni$/C, and our $Pt_{73}Ni_{27}$/C. The durability tests for these catalysts were not based on the same ADT procedure (Table 1).

make strict and accurate comparisons mutually among the durability data because of a variety of the ADT conditions in the literature. Nevertheless, the comparison with the literature would provide useful and convincing information on the stability issue because our catalyst possessed a remarkable durability as

shown in Figure 3. In this study we have examined the durability of our catalyst by an ADT protocol of the Fuel Cell Commercialization Conference of Japan (FCCJ) as described in Experimental.

2. Key factors for the simultaneous increase in the activity and durability of the octahedral $Pt_{73}Ni_{27}/C$. At the initial stage of the reduction of the Pt and Ni precursors during octahedral $PtNi_x$ synthesis, small crystal nuclei of Pt as a main component are regarded to form hexapod-like concave nanocrystals, exposing different crystal planes such as {110}, {100}, and {111} with different surface energies.[26,39] Similar phenomena of Pt-rich phase segregation to edges during the synthesis of $PtNi_3$ and $PtCo_3$ rhombic dodecahedra in oleylamine were observed and the element manipulation in the rhombic dodecahedra or nanoframes was fully described.[41,44,57] The under-potential deposition of Ni may occur preferably on Pt {111} due to the lower surface energy/favorable energy barrier, which may bring about the formation of octahedral shape and Ni segregated {111} facets. Recent reports revealed that the migration of Pt from nuclei to surface also occurs to form a Pt-rich surface during the nanocrystal growth.[36,39,41] As well known, the electrochemical reactivity of Ni metal is higher than that of Pt metal due to the standard electrode potentials, $Ni^{2+}/Ni < Pt^{2+}/Pt$. In the present study using MF as a reduction agent in the presence of PVP, Ni^{2+} ions are reduced by MF to Ni metal atoms, and a part of Pt^{2+} ($Pt(acac)_2$) is probably reduced by Ni metal on the {111} facets besides the reduction with MF, resulting in preferential growth of the {111} crystal planes to form the as-synthesized octahedral $Pt_{50}Ni_{50}/C$. During the activating treatment Ni atoms in the $Pt_{50}Ni_{50}/C$ are eluted to produce the concave octahedral $Pt_{73}Ni_{27}/C$ with three Pt skin surfaces as discussed hereinafter.

The average particle sizes of the as-synthesized, activated and ADT (10,000 cycles) $PtNi_x/C$ samples were 14.0±1.97 nm, 13.2±2.15, and 13.6±1.50 nm, respectively (Figure S3). No particle growth occurred by the 10,000 ADT cycles. The bulk composition of Pt and Ni atoms in the as-synthesized $PtNi_x/C$ was estimated to be $Pt_{50}Ni_{50}$ by ICP-AES and XRF. STEM images in a high angle annular dark field (HAADF) mode for the as-synthesized $Pt_{50}Ni_{50}/C$ (Figure 4 and Figure S4) indicate an octahedral structure with {111} facet planes. The HAADF STEM contrasts and EDS Pt/Ni maps in Figure 4 (a), (b), (c), (d) and (f) show a symmetric and anisotropic distribution of Pt and Ni atoms at vertexes, edges, and {111} facets. The EDS line analysis in Figure 4 (d) and (e) exhibit a concave shape at the {111} facets. Around the vertex Pt (57%) was more abundant than Ni (43%) and at both edges Pt was also more rich than Ni, while at the {111} facets Ni (60%) was much more than Pt (40%) (Figure 4 (b)), where the element distribution

was nearly symmetric. Pt atoms were located more at the vertexes and edges, while Ni atoms were located more around the {111} facets like domains. These segregated Ni atoms around the {111} facets in the as-synthesized octahedral $Pt_{50}Ni_{50}$/C are not exposed significantly to the nanoparticle surface as proved by negligible XPS Ni 2p signals in Figure S5. The negligible Ni is not due to low particle coverage and signal because the intensity of Pt 4f signals in the survey spectra is similar to that for as-purchased Pt/C (TEC10E20E) and strong enough to exclude the possibility of low particles coverage and signal. It is suggested from the photoelectron inelastic escape depth in metals that at least three Pt-skin layers with little Ni atoms cover the octahedral nanoparticles. The results add credence to the CO/Hupd result above mentioned. It is different from other as-synthesized Pt–Ni/C samples reported previously, where a significant amount of Ni^{2+} ions (probably NiO) at the surfaces was observed by XPS.[37,40,58] The binding energies of Pt $4f_{7/2}$ and $4f_{5/2}$ levels for the as-synthesized $Pt_{50}Ni_{50}$/C were 71.0 eV and 74.3 eV, which are lower by 0.5 eV than those (71.5 eV and 74.8 eV, respectively) for Pt foil. The Pt 4f binding energies for the Pt skin layers of the activated $Pt_{73}Ni_{27}$/C and ADT $Pt_{74}Ni_{26}$/C catalysts shifted back to those of Pt foil due to the Ni dissolution. The present synthesis method preferentially produced Pt skin layers on the octahedral nanoparticles without any additional treatments. Figure 4 (d) and (e) are the atomic scale topographic STEM-EDS analysis for the interplane spacing of the as-synthesized octahedral $Pt_{50}Ni_{50}$/C in

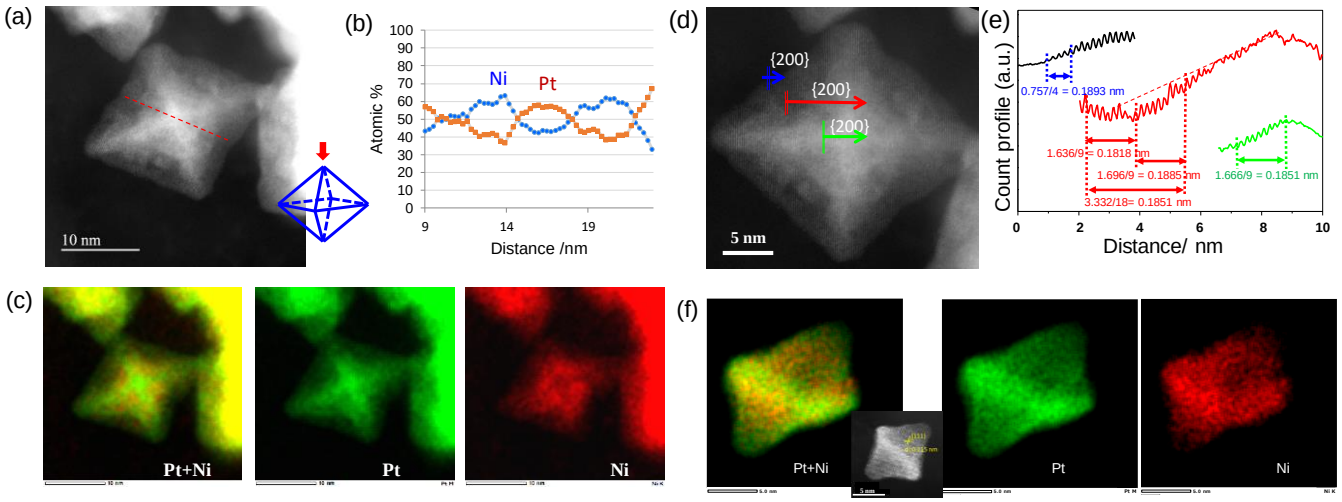

Figure 4. HAADF STEM images, EDS line profile, EDS element mappings, and atomic-scale topographic STEM-EDS line analysis for as-synthesized octahedral $Pt_{50}Ni_{50}$/C. (a): STEM image. (b): EDS atomic % profile in the red dashed line of (a) for Pt and Ni. (c): Pt and Ni EDS maps of the same PtNi nanoparticle as (a) (scale bars: 5 nm). (f): Pt and Ni EDS maps of another single PtNi nanoparticle (inserted STEM) viewed in a different direction. (d, e): Compressive strain estimated by the atomic-scale topographic STEM-EDS analysis for the d(200) spacing. (e): The red and green dashed lines show the (111) facet plane slope and edge slope along the red and green arrows in (d).

the (200) direction to estimate the compressive strain of the surface Pt layers. The d(200) spacings near the side edge and vertex were 0.1893 nm and 0.1851 nm, respectively, which are compressive by 3.5% and 5.6%, respectively compared to that in Pt bulk (0.1962 nm). A place near the {111} facet center (0.1818 nm) showed 7.3 % compression. The most compressive strain at the {111} facet is conceived to be due to the underlying Ni-rich domain (d(200) spacing of Ni bulk: 0.1762 nm) as mapped in Figure 4 (c) and (f) (see Figure S6 for the d(111) spacings). The surface stress of the three Pt skin layers of the as-synthesized $Pt_{50}Ni_{50}$ nanoparticles was larger than that of the three Pt skin layers of the activated $Pt_{73}Ni_{27}$ and ADT $Pt_{74}Ni_{26}$ nanoparticles as discussed hereinafter. In this study we assumed that the surface stress of the three Pt skin layers in the octahedral $PtNi_x$ nanoparticles with 13-14 nm dimension is brought mainly from the underlying Pt-Ni alloy/intermetallic cores, and we estimated the compressive strains relative to the Pt bulk lattice parameters as reference states.

The HAADF STEM image of Figure 5 for the activated $PtNi_x$/C evidences the retention of the octahedral framework after the activating treatment. In both side-edge regions (0.81 nm) the major element was Pt, and Ni atoms were few. The distance of 0.81 nm corresponds to 3.0 Pt skin layers taking into account the direction of the line profile deviated by 42.5^o from the d(200) direction. The Pt/Ni composition estimated by the XRF analysis was $Pt_{73}Ni_{27}$, which was similar to the composition ($Pt_{80}Ni_{20}$) estimated from the XRD (220) peak within the error range. Figure 5 (c) is the Pt and Ni EDS maps of the same $Pt_{73}Ni_{27}$ nanoparticle as (a), which demonstrates that both Pt and Ni atoms are distributed anisotropically and symmetrically. It is to be noted that the Pt and Ni maps are viewed to be superimposed to each other, showing similar distribution of both Pt and Ni atoms in a crystallite.

It is notable that the compressive stress in the as-synthesized $Pt_{50}Ni_{50}$/C was partially released in the activated octahedral $Pt_{73}Ni_{27}$/C (Figure 5 (d) and (e)). The compressive strains of the edges, vertexes and {111} facets averaged on the d(200) and d(111) spacings in the activated $Pt_{73}Ni_{27}$/C electrocatalyst are listed in Table 2 (Table S1 in more detail). In the as-synthesized $Pt_{50}Ni_{50}$/C the compressive strains at the

Table 2. Compressive strains averaged on the d(200) and d(111) spacings by HAADF STEM analysis

	as-synthesized $Pt_{50}Ni_{50}$/C	activated $Pt_{73}Ni_{27}$/C	ADT $Pt_{74}Ni_{26}$/C
Compressive strain	**%**	**%**	**%**
Edge	**3.6**	**2.6**	**2.5**
vertex	**5.4**	**3.6**	**3.4**
{111} facet	**6.7**	**2.0**	**2.1**

Error range: ±1%

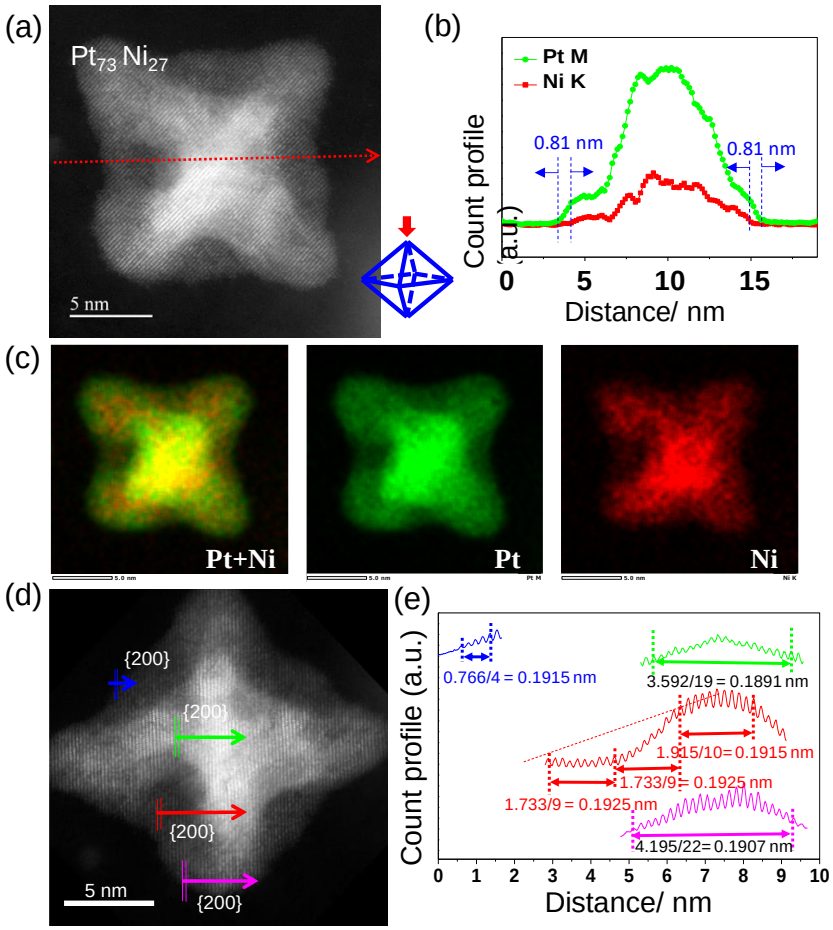

Figure 5. HAADF STEM images, EDS line profile, EDS element mappings, and atomic-scale topographic STEM-EDS line analysis for activated octahedral $Pt_{73}Ni_{27}$/C. (a): STEM image. (b): EDS atomic % profile in the red dashed line of (a) for Pt and Ni. (c): Pt and Ni EDS maps of the same PtNi nanoparticle as (a) (scale bars: 5 nm). (d, e): Compressive strain estimated by the atomic-scale topographic STEM-EDS analysis for the d(200) spacing. (e): The red dashed line shows the (111) facet plane slope along the red arrow in (d).

edges, vertexes and {111} facets were 3.6%, 5.4% and 6.7%, respectively on average of the d(200) and d(111) spacings (Table 2 and Table S1). The composition changed from $Pt_{50}Ni_{50}$/C to $Pt_{73}Ni_{27}$/C by the activating treatment in 0.1 M $HClO_4$, while keeping the octahedral structure as shown in Figure 5. In the $Pt_{73}Ni_{27}$/C the compressive strains at the edges, vertexes and {111} facets were 2.6%, 3.6% and 2.0%, respectively (Table 2 and Table S1). The Pt/Ni composition of the bimetal core in the $Pt_{73}Ni_{27}$ nanoparticles was estimated to be $Pt_{67}Ni_{33}$ (Pt/Ni=2/1) by taking into account the three Pt skin layers and 13.2 nm dimension.

The Ni leaching occurred preferentially from the {111} facets as suggested by the EDS maps in Figure 4 and Figure 5 and also by the largest release of the surface stress at the {111} facets among the edges, vertexes and {111} facets in Table 2 though the Ni leaching also occurred a little from the edges and vertexes. The Ni leaching accompanied with the partial release of the compressive stress brought about a concave feature in the {111} facet planes and at the edges (Figure 6), which is another important structure change in the surface geometry. The concave domain-size and depth in the {111} facet planes became larger and more distinct for the activated $Pt_{73}Ni_{27}/C$ compared to those for the as-synthesized $Pt_{50}Ni_{50}/C$ as shown in Figure 4 (e) and Figure 5 (e). The remarkable concave structure in the {111} facet planes of the octahedral $Pt_{73}Ni_{27}$ nanoparticles (Figure 6 (c, d) produced the exposed (110) and (001) facets

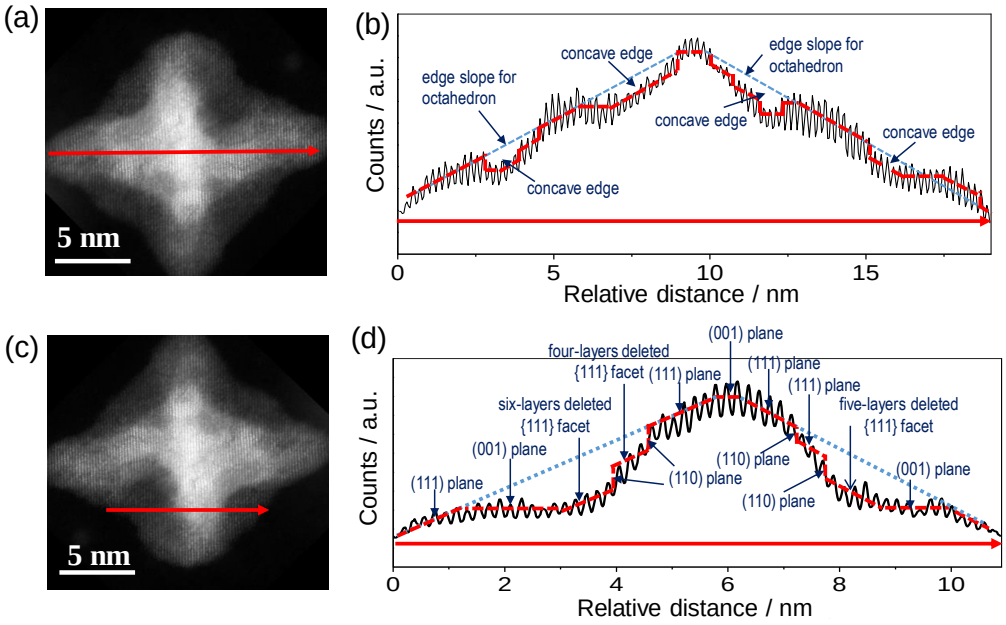

Figure 6. Cross-section gray-values along with red lines in the STEM images for the activated octahedral Pt73Ni27/C and the concave features. (a, b) Cross-section edge profile. (c, d) Cross-section {111} facet profile.

besides the exposed (111) facets and provided concave defects. Calle-Valleo et al.[62-65] theoretically demonstrated that the steps located in concave nanostructures contain active concave defects with high coordination of Pt atoms at the step bottom and inactive convex defects with under coordination of Pt atoms at the step edge. They also revealed that the highly-coordinated concave defects have the smaller oxygen adsorption energy than the corresponding flat (111) plane and their ORR activity can surpass that of the flat (111) surface. [62-65] Our experimental results may provide an evidence to the theoretical

calculations. It was also reported by Dubau et al.[66,67] and Chattot et al.[68] that the overall activity of the concave nanostructured surface can exceed the flat (111) surface though there are the less active convex defects in the concave nanostructured surface. The concave nanostructured surface may prevent from forming and adsorbing of strong (e.g. six-ring) water clusters at the {111} facet planes of the octahedral $Pt_{73}Ni_{27}$ nanoparticles, which can also promote the ORR performance of the octahedral $Pt_{73}Ni_{27}$ nanoparticles.

In contrast to the surface sensitive XPS data, the *in situ* Pt L_3-edge XANES spectra, which provide electronic information averaged on all Pt atoms involved in the $Pt_{73}Ni_{27}$/C, showed the smaller intensity of the white line peak (2p→5d transition) than that for the Pt/C (TEC10E50E-HT). It indicates an electronic modification of Pt atoms in the $Pt_{67}Ni_{33}$ alloy core by Ni atoms. The CO stripping peak, which is lower by 100 mV from that for Pt/C (Figure 2 (a) and (b)), suggests the much weaker adsorption of oxygenated species on the three Pt skin layers of the activated octahedral $Pt_{73}Ni_{27}$/C than on the Pt/C. We

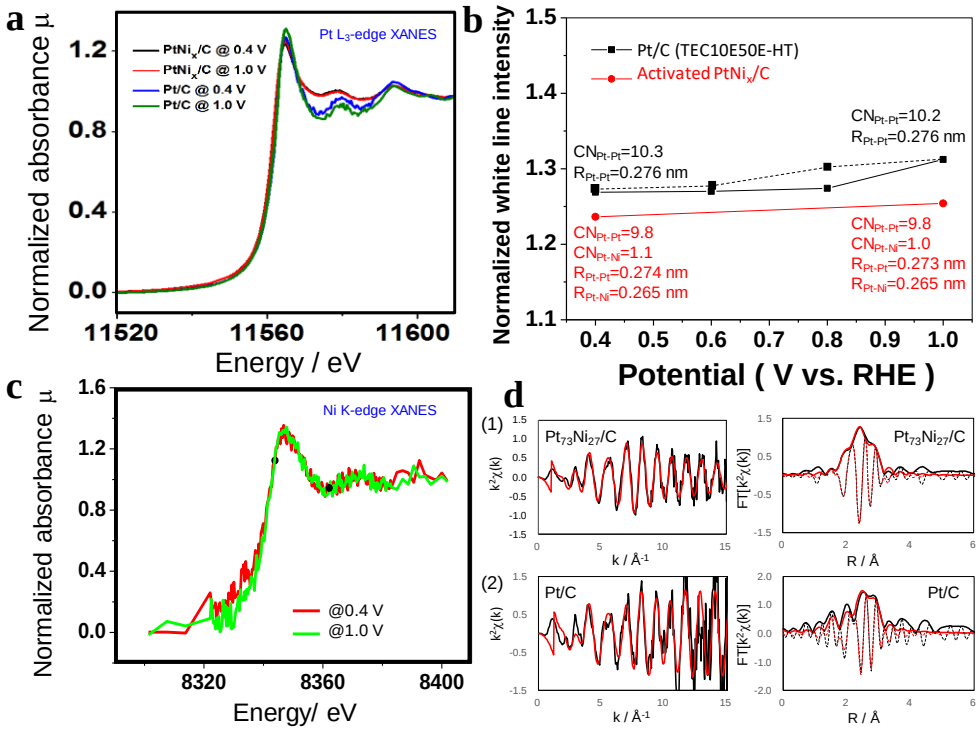

Figure 7. (a) *In situ* Pt L_3-edge XANES spectra for the activated Pt/C (TEC10E50E-HT) and octahedral $Pt_{73}Ni_{27}$/C at 0.4 and 1.0 V_{RHE} in N_2-saturated 0.1 M $HClO_4$. (b) Comparison of the XANES white line peak intensities for the Pt/C and $Pt_{73}Ni_{27}$/C at 0.4 V_{RHE} -1.0 V_{RHE}. Solid line: 0.4 V_{RHE} --→ 1.0 V_{RHE}. Dotted line: 1.0 V_{RHE} --→ 0.4 V_{RHE}. (c) *In situ* Ni K-edge XANES spectra for the activated octahedral $Pt_{73}Ni_{27}$/C at 0.4 and 1.0 V_{RHE} in N_2-saturated 0.1 M $HClO_4$. (d) *In situ* Pt L_3-edge EXAFS oscillations and Fourier transforms for the activated Pt/C (1) and octahedral $Pt_{73}Ni_{27}$/C (2) at 1.0 V_{RHE} in N_2-saturated 0.1 M $HClO_4$.

have conducted *in situ* XAFS measurements to evidence the weak adsorption of oxygenated species and compressive strain of the Pt skin layers of the octahedral structure *in situ* under the potential operating conditions from 0.4 V_{RHE} to 1.0 V_{RHE} by using a home-made XAFS cell.[15] Figure 7 (a) shows *in situ* Pt L_3-edge XANES spectra for the activated Pt/C (TEC10E50E-HT) and octahedral $Pt_{73}Ni_{27}$/C at 0.4 V_{RHE} and 1.0 V_{RHE} in N_2-saturated 0.1 M $HClO_4$. For the octahedral core-shell $Pt_{73}Ni_{27}$/C the white line intensity (metallic Pt valence) did not change significantly by increasing the voltage from 0.4 V_{RHE} to 1.0 V_{RHE} (Figure 7 (b)) and the *in situ* Pt L_3-edge EXAFS analysis revealed only the Pt-Pt bond and no Pt-O bonds were observed at 0.4 – 1.0 V_{RHE} (Figure S9 and Table S3). The absence of definite Pt-O bonds in *in situ* Pt L_3-edge EXAFS analysis may be contrasted to the presence of the oxygen desorption peak at the relatively higher potential in the CV for the $Pt_{73}Ni_{27}$/C. These results demonstrate that strongly bound oxygen species on the $Pt_{73}Ni_{27}$/C is few compared to the case of the Pt/C surface and most surface adsorbed oxygen species are disordered without making Pt-O bonds at a definite distance. The results on the active $Pt_{73}Ni_{27}$/C are entirely different from those for the Pt/C, which showed the increase in the white line intensity above 0.8 V_{RHE} and the existence of Pt-O bonds at 0.195±0.006 nm in addition to Pt-Pt bonds at 1.0 V_{RHE} (Figure 7 (d), Figures S8 and Tables S2). The averaged Pt valence in the Pt/C is estimated to be about 0.2+ at 1.0 V_{RHE}.

For the $Pt_{73}Ni_{27}$/C only Pt-Pt and Pt-Ni bonds were observed at 0.274 nm (CN_{Pt-Pt}: 9.8± 0.7) and 0.265 nm (CN_{Pt-Ni}:1.1± 0.5), respectively at 0.4 V_{RHE} and at 0.273 nm (CN_{Pt-Pt}: 9.8± 0.7) and 0.265 nm (CN_{Pt-Ni}:1.0± 0.5), respectively at 1.0 V_{RHE}. The similar structural parameters at 0.4 V_{RHE} and 1.0 V_{RHE} prove the remarkable stability of the octahedral $Pt_{73}Ni_{27}$/C under the potential operating conditions. The *in situ* Pt-Pt bond distance (0.273-0.274 nm) is significantly shorter than Pt bulk (0.2775 nm), which shows 1.6% (±0.4%) compression. The value agrees with the compressive strain (2.0%) of the {111} facets of the major area in the octahedral structure estimated by the STEM d spacing analysis. Figure 7 (c) shows *in situ* Ni K-edge XANES spectra for the activated octahedral $Pt_{73}Ni_{27}$/C at 0.4 and 1.0 V_{RHE} in N_2-saturated 0.1 M $HClO_4$. Both XANES spectra were almost same. If Ni atoms are exposed to the surface, they should be oxidized at 1.0 V_{RHE}. Hence, the Ni K-edge XANES also evidences no existence of Ni atoms at the surface in agreement with the Ni 2p XPS data in Figure S5. The tightening Pt skin layers prevent Ni oxidative leaching from the bulk.

It is also notable that the $Pt_{67}Ni_{33}$ bimetal core in the activated octahedral $Pt_{73}Ni_{27}$/C is an intermetallic phase rather than a random alloy phase as suggested by the coordination number of Pt-Pt and Pt-Ni bonds. If the $Pt_{67}Ni_{33}$ bimetal core in the activated octahedral $Pt_{73}Ni_{27}$/C has a random alloy phase, the Pt-Ni bond

distance would be similar to the Pt-Pt bond distance and the Pt-Ni coordination number would be expected to be 2.8. Actually, the coordination number of Pt-Ni bonds at 0.265 nm was determined to be as small as 1.1 (Figure S9 and Table S3). Thus, the core may be an intermetallic phase rather than a random alloy phase. The $Pt_{67}Ni_{33}$ intermetallic core induces the surface-compressive strain of the three Pt skin layers, resulting in undetectable oxygen adsorption on the Pt surface as suggested by the in situ XAFS analysis. The weaker oxygen binding strength promotes the ORR performance of the octahedral $Pt_{73}Ni_{27}$ surface minimizing the surface coverage of interfering unreactive oxygenate species. The $Pt_{67}Ni_{33}$ intermetallic core induces the surface-compressive strain of the three Pt skin layers, minimizing the surface coverage of interfering unreactive oxygenate species.

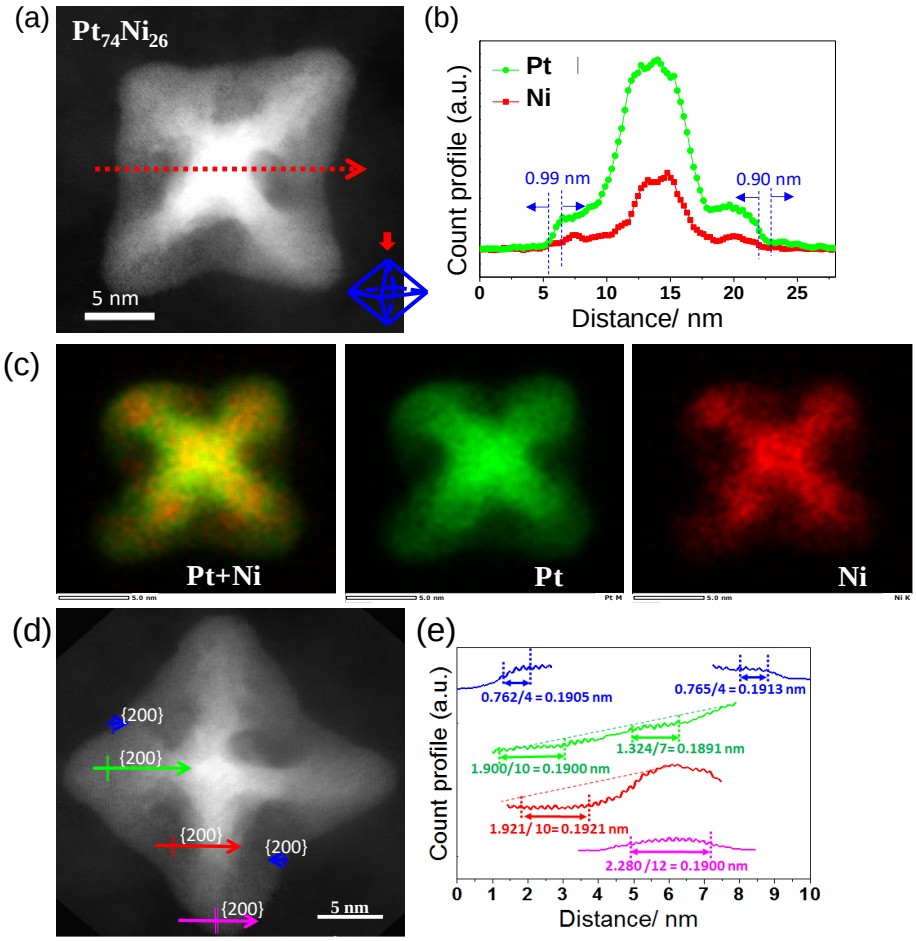

Figure 8. HAADF STEM images, EDS line profile, EDS element mappings, and atomic-scale topographic STEM-EDS line analysis for ADT (10,000 cycles) octahedral $Pt_{74}Ni_{26}$/C. (a): STEM image. (b): EDS atomic % profile in the red dashed line of (a) for Pt and Ni. (c): Pt and Ni EDS maps of the same PtNi nanoparticle as (a) (scale bars: 5 nm). (d, e): Compressive strain estimated by the atomic-scale topographic STEM-EDS analysis for the d(200) spacing. (e): The red and green dashed lines show the (111) facet plane slope and edge slope along the red and green arrows in (d), respectively.

The remarkable property of the activated octahedral $Pt_{73}Ni_{27}$/C electrocatalyst is the robust performance to show high activity and durability simultaneously. The high durability of the $Pt_{73}Ni_{27}$/C is significantly different from the previous octahedral $PtNi_x$/C electrocatalysts,[37,40,45,46] which had high initial activity but suffered serious activity decay due to collapse of the octahedron to a near-sphere shape by the ADT load cycles.[37,45] The HAADF STEM images of Figure 8 (a) and (d) and Figure S7 for the ADT(10,000 cycles) $PtNi_x$/C indicate the retention of the octahedral framework after the ADT 10,000 cycles. The Pt and Ni EDS line profiles in Figure 8 (b) exhibited nearly symmetric distribution of Pt and Ni atoms in a single $PtNi_x$ nanoparticle, also indicating the octahedral structure. In both edge regions (0.90-0.99 nm) of Figure 8 (b) the major element was Pt, and the distances of 0.90-0.99 nm correspond to 3.1-3.4 Pt skin layers, which also agrees with the Ni XPS results. The Pt/Ni composition estimated by ICP-AES and XRF analysis was $Pt_{74}Ni_{26}$. Figure 8 (c) is the Pt and Ni EDS maps of the same $Pt_{74}Ni_{26}$ nanoparticle as Figure 8 (a), which demonstrates that the Pt and Ni atoms are distributed in the similar anisotropy and symmetry to each other in a crystallite. It should be noted that the octahedral framework and Pt/Ni composition of the activated $Pt_{73}Ni_{27}$/C remained almost unchanged after the ADT 10,000 cycles. In the ADT $Pt_{74}Ni_{26}$/C sample the compressive strains at the edges, vertexes and {111} facets were 2.5%, 3.4% and 2.1% on average, respectively, which are almost the same as those for the activated $Pt_{73}Ni_{27}$/C, confirming the stability of the octahedral $Pt_{73}Ni_{27}$/C structure (Figure 8 (e), Table 2 and Table S1). The durability of the $Pt_{73}Ni_{27}$/C structure is also confirmed by the similar concave {111} facet surfaces in Figure 5 (e) and Figure 8 (e).

According to the detailed structure information, the origin of the robust stability of the activated octahedral $Pt_{73}Ni_{27}$/C is elaborated as follows. The continuous, 2.0-3.6% compressive and concave Pt skin layers with the concave defects and high Pt coordination have a high Pt oxidation potential and effectively prevent from Ni leaching out during long-term ADT cycles, which is also a key structure to generate and maintain the high activity. The concave structure may reduce the strong adsorption of oxygen species and water clusters under the ORR conditions. The underlying intermetallic $Pt_{67}Ni_{33}$ core and symmetric element distribution may also be important for keeping the continuity and completeness of the three Pt skin layers. Otherwise, over-strained points/zones at Pt skin layers would probably be destroyed and the nanostructure would collapse during repeated ADT cycles.

3. Structural transformation of the as-synthesized octahedral $Pt_{50}Ni_{50}$ to the activated octahedral $Pt_{73}Ni_{27}$ by the partial release of the compressive strain and the dimension reduction. In consequence

of the above results a scheme for the formation of the activated core-shell $Pt_{73}Ni_{27}$/C structure from the as-synthesized $Pt_{50}Ni_{50}$/C structure by Ni leaching and Pt filling is illustrated in Figure 9. The seamless three Pt skin layers prevent from further leaching Ni atoms of the intermetallic core as proved by a negligible change in the $Pt_{73}Ni_{27}$ composition after the ADT 10,000 cycles as well as from deterioration of the octahedral structure. However, it has been demonstrated that even if Ni atoms are located in the core part surrounded by Pt shells, the Ni leaching still proceeds accompanied with the disappearance and deterioration of the shape/facet.[37,45,69] Thus, it is suggested that the new robust property of the activated octahedral $Pt_{73}Ni_{27}$/C electrocatalyst originates from a partial release of the compressive strain from 5.4% to 3.6% at the vertexes, from 3.6% to 2.6% at the edges, and particularly from 6.7% to 2.0% at the {111}

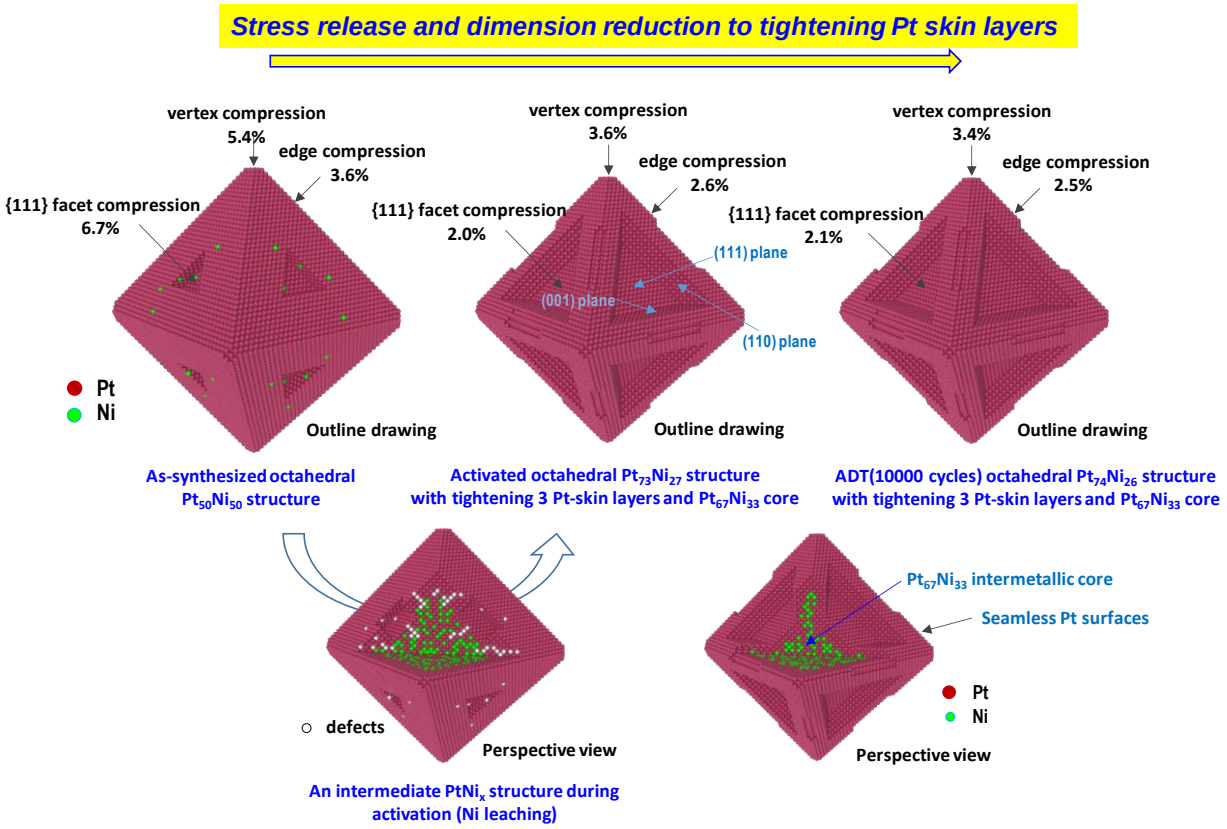

Figure 9. Illustration for the octahedral $Pt_{50}Ni_{50}$, $Pt_{73}Ni_{27}$ and $Pt_{74}Ni_{26}$ nanoparticle structures (outside 3D drawing) in the as-synthesized, activated and ADT(10,000 cycles) $PtNi_x$/C cathode catalysts, respectively. An intermediate structure (perspective viewing) during the activating treatment (Ni leaching) is also illustrated. A perspective viewing of the activated and ADT catalysts is also illustrated to show the $Pt_{67}Ni_{33}$ intermetallic core. The activated $Pt_{73}Ni_{27}$/C possesses tightening three Pt skin layers with 2.0-3.6% compressive strains, a $Pt_{67}Ni_{33}$ intermetallic core and a symmetric Pt/Ni distribution, which was produced by the partial release of the stress, Pt/Ni rearrangement and dimension reduction of the as-synthesized octahedral $Pt_{50}Ni_{50}$/C with 3.6-6.7% compressive Pt skin layers by Ni leaching during the activation process.

facets during the Ni leaching from the as-synthesized octahedral $Pt_{50}Ni_{50}$/C in the activating process, where the Ni leaching may preferentially proceed from the {111} facets, while keeping the concave octahedral framework. The preferential Ni leaching from the {111} facets produced a concave feature with exposed (110) facets and high-coordination concave defects besides exposed (111) and (001) facets in the {111} facet planes, which can explain so high activity of the octahedral $Pt_{73}Ni_{27}$/C (Figure 6).[62-65] The transformation of the as-synthesized octahedral $Pt_{50}Ni_{50}$/C to the activated octahedral $Pt_{73}Ni_{27}$/C is subjected to the tensile Pt spacing and rearrangement of several surface layers to fill vacancies left behind the Ni leaching and the dimension reduction from 14.0 nm to 13.2 nm. The partial release of the stress and dimension reduction occur symmetrically to maintain the octahedral $PtNi_x$ structure with the three Pt skin layers without its deterioration. Thus, the octahedral $Pt_{73}Ni_{27}$/C with the continuous, 2.0-3.6% compressive and concave Pt skin layers, the $Pt_{67}Ni_{33}$ intermetallic core and the symmetric Pt/Ni distribution are totally regarded as key issues to enhance both the ORR activity and long-term durability of the $PtNi_x$/C electrocatalyst. Better control of catalytic architecture has made possible the preparation of electrocatalytic materials with enhanced activity and stability.

Finally, when the catalyst is applied to a practical MEA though it is not a topic of the manuscript, the electrochemical activation may bring about a possible contamination of the MEA membrane from Ni leaching. L. Dubau et al. examined the effect of annealing treatments of an as-synthesized hollow $PtNi_x$/C under different conditions and found that the annealing under N_2 was better than under H_2 or air though the activity still decreased a little from the as-synthesized hollow $PtNi_x$/C.[66,67] Appropriate annealing of the catalyst powder prior to its inclusion to the MEA may be more desirable practically if the structured $PtNi_x$ surface can be fabricated.

CONCLUSIONS

The simultaneous improvement of the ORR activity and durability was achieved with the octahedral $Pt_{73}Ni_{27}$/C catalyst. We found a strategic fabrication using metal precursors, $Pt(acac)_2$ and $Ni(acac)_2$ with a 1:1 ratio in DMF solvent, an adjusted amount of methyl formate (MF) as a reducing agent, and polyvinyl pyrrolidone (PVP) as a capping agent to synthesize octahedral $Pt_{50}Ni_{50}$ nanoparticles with a symmetric distribution of Pt (located more at edges and vertexes) and Ni elements (located more at {111} facets). The as-synthesized octahedral $Pt_{50}Ni_{50}$/C with the compressive strains of 5.4% at the vertexes, 3.6% at the edges and 6.7% at the {111} facets was activated to the octahedral $Pt_{73}Ni_{27}$/C catalyst by symmetric Ni leaching preferentially from the {111} facet planes accompanied with the tensile rearrangement and

dimension reduction by complete vacancy filling with Pt atoms at the surface layers to form the continuous and concave Pt skin layers electronically modified from the $Pt_{67}Ni_{33}$ intermetallic core. The continuous and concave nanostructured Pt skin layers in the octahedral $Pt_{73}Ni_{27}$ structure possess the 2.0-3.6% compressive strains and concave defects with high Pt coordination, which may minimize the surface coverages of interfering unreactive oxygenate species and strongly-adsorbed water clusters under the ORR conditions. The continuous, 2.0-3.6% compressive and concave $Pt_{73}Ni_{27}$/C brought about the simultaneous improvement of the remarkable level ORR activity (mass activity and surface specific activity: 6.8-16.9 and 20.3-24.0 times larger than Pt/C, respectively) and long-term durability (negligible loss after 10,000 ADT cycles). The composition and structure of the octahedral core-shell $Pt_{73}Ni_{27}$/C remained almost unchanged after 10,000 ADT load cycles. The present results on the better control of robust catalytic architecture provide a new insight into development of next-generation PEFC cathode catalysts and renew the current knowledge and viewpoint for instability of octahedral $PtNi_x$/C samples

ASSOCIATED CONTENT

Electronic Supplementary Information (ESI) available via the Internet at http://pubs.acs.org.

The TEM/STEM, XPS, lattice contrast profiles, XANES, and EXAFS data.

AUTHOR INFORMATION

Corresponding Author

* Yasuhiro Iwasawa

Tel: +81-42-443-5921; E-mail: iwasawa@pc.uec.ac.jp

Author Contributions

The manuscript was written through contributions of all authors. All authors have given approval to the final version of the manuscript.

Funding Sources

The New Energy and Industrial Technology Development Organization (NEDO) of the Ministry of Economy, Trade, and Industry (METI), Japan.

ACKNOWLEDGMENT

The XAFS measurements were performed with the approval of SPring-8 subject number 2013B7802, 2014A7800, 2014A7805, 2014B7800, 2015A7800, 2015A7803, 2015B7800, 2016A7800, 2016B7800. This work was supported by the New Energy and Industrial Technology Development Organization (NEDO) of the Ministry of Economy, Trade, and Industry (METI), Japan.

REFERENCES

(1) Debe, M. K. *Nature* **2012,** *486*, 43-51.

(2) Rabis, A.; Rodriguez, P.; Schmidt, T. J. *ACS Catal.* **2012,** *2*, 864-890.

(3) Borup, R.; Meyers, J.; Pivovar, B.; Kim, Y. S.; Mukundan, R.; Garland, N.; Myers, D.; Wilson, M.; Garzon, F.; Wood, D.; Zelenay, P.; More, K.; Stroh, K.; Zawodzinski, T.; Boncella, J.; McGrath, J. E.; Inaba, M.; Miyatake, K.; Hori, M.; Ota, K.; Ogumi, Z.; Miyata, S.; Nishikata, A.; Siroma, Z.; Uchimoto, Y.; Yasuda, K.; Kimijima, K.-i.; Iwashita, N. *Chem. Rev.* **2007,** *107*, 3904-3951.

(4) Stamenkovic, V. R.; Fowler, B.; Mun, B. S.; Wang, G. F.; Ross, P. N.; Lucas, C. A.; Markovic, N. M. *Science* **2007,** *315*, 493-497.

(5) Strasser, P.; Koh, S.; Anniyev, T.; Greeley, J.; More, K.; Yu, C.; Liu, Z.; Kaya, S.; Nordlund, D.; Ogasawara, H.; Toney, M. F.; Nilsson, A. *Nature Chem.* **2010,** *2*, 454-460.

(6) Wang, D.; Xin, H. L.; Hovden, R.; Wang, H.; Yu, Y.; Muller, D. A.; DiSalvo, F. J.; Abruña, H. D. *Nat Mater* **2013,** *12*, 81-87.

(7) Wu, J.; Yang, H. *Acc. Chem. Res.* **2013,** *46*, 1848-1857.

(8) Dresselhaus, M. S.; Thomas, I. L. *Nature* **2001,** *414*, 332-337.

(9) Weber, A. Z.; Newman, J. *Chem. Rev.* **2004,** *104*, 4679-4726.

(10) Wang, C.-Y. *Chem. Rev.* **2004,** *104*, 4727-4766.

(11) Jacobson, M. Z.; Colella, W. G.; Golden, D. M. *Science* **2005,** *308*, 1901-1905.

(12) Steele, B. C. H.; Heinzel, A. *Nature* **2001,** *414*, 345-352.

(13) Stamenkovic, V.; Mun, B. S.; Mayrhofer, K. J. J.; Ross, P. N.; Markovic, N. M.; Rossmeisl, J.; Greeley, J.; Norskov, J. K. *Ange. Chem. Int. Ed.* **2006,** *45*, 2897-2901.

(14) Shao, Z.; Haile, S. M.; Ahn, J.; Ronney, P. D.; Zhan, Z.; Barnett, S. A. *Nature* **2005,** *435*, 795-798.

(15) Nagasawa, K.; Takao, S.; Nagamatsu, S.-i.; Samjeské, G.; Sekizawa, O.; Kaneko, T.; Higashi, K.; Yamamoto, T.; Uruga, T.; Iwasawa, Y. *J. Am. Chem. Soc.* **2015,** *137*, 12856-12864.

(16) Sha, Y.; Yu, T. H.; Merinov, B. V.; Shirvanian, P.; Goddard, W. A. *J. Phys. Chem. Lett.* **2011,** *2*, 572-576.

(17) Stephens, I. E. L.; Bondarenko, A. S.; Gronbjerg, U.; Rossmeisl, J.; Chorkendorff, I. *Energy Environ. Sci.* **2012,** *5*, 6744-6762.

(18) Zhang, J.; Lima, F. H. B.; Shao, M. H.; Sasaki, K.; Wang, J. X.; Hanson, J.; Adzic, R. R. *J. Phys. Chem. B* **2005,** *109*, 22701-22704.

(19) Chen, Y.; Liang, Z.; Yang, F.; Liu, Y.; Chen, S. *J. Phys. Chem. C* **2011,** *115*, 24073-24079.

(20) Yang, H. *Angew. Chem. Int. Ed.* **2011,** *50*, 2674–2676.

(21) Zhang, J.; Mo, Y.; Vukmirovic, M. B.; Klie, R.; Sasaki, K.; Adzic, R. R. *J. Phys. Chem. B* **2004,** *108*, 10955-10964.

(22) Sasaki, K.; Naohara, H.; Cai, Y.; Choi, Y. M.; Liu, P.; Vukmirovic, M. B.; Wang, J. X.; Adzic, R. R. *Angew. Chem. Int. Ed.* **2010,** *49*, 8602-8607.

(23) Zhang, J.; Vukmirovic, M. B.; Xu, Y.; Mavrikakis, M.; Adzic, R. R. *Angew. Chem. Int. Ed.* **2005,** *44*, 2132-2135.

(24) Zhang, J. L.; Vukmirovic, M. B.; Sasaki, K.; Nilekar, A. U.; Mavrikakis, M.; Adzic, R. R. *J. Am. Chem. Soc.* **2005,** *127*, 12480-12481.

(25) Li, M.; Zhao, Z.; Cheng, T.; Fortunelli, A.; Chen, C.-Y.; Yu, R.; Zhang, Q.; Gu, L.; Merinov, B.; Lin, Z.; Zhu, E.; Yu, T.; Jia, Q.; Guo, J.; Zhang, L.; Goddard, W. A.; Huang, Y.; Duan, X. *Science* **2016**, *354*, 1414-1419.

(26) Gan, L.; Cui, C.; Heggen, M.; Dionigi, F.; Rudi, S.; Strasser, P. *Science* **2014,** *346*, 1502-1506.

(27) Kibler, L. A.; El-Aziz, A. M.; Hoyer, R.; Kolb, D. M. *Angew. Chem. Int. Ed.* **2005,** *44*, 2080-2084.

(28) Mavrikakis, M.; Hammer, B.; Nørskov, J. K. *Phys. Rev. Lett.* **1998,** *81*, 2819-2822.

(29) Kitchin, J. R.; Nørskov, J. K.; Barteau, M. A.; Chen, J. G. *Phys. Rev. Lett.* **2004,** *93*, 156801.

(30) Small, M. W.; Kas, J. J.; Kvashnina, K. O.; Rehr, J. J.; Nuzzo, R. G.; Tromp, M.; Frenkel, A. I. *ChemPhysChem* **2014,** *15*, 1569-1572.

(31) Liu, L.; Samjeské, G.; Takao, S.; Nagasawa, K.; Iwasawa, Y. *J. Power Sources* **2014,** *253*, 1-8.

(32) Becknell, N.; Kang, Y.; Chen, C.; Resasco, J.; Kornienko, N.; Guo, J.; Markovic, N. M.; Somorjai, G. A.; Stamenkovic, V. R.; Yang, P. *J. Am. Chem. Soc.* **2015,** *137*, 15817-15824.

(33) Nesselberger, M.; Roefzaad, M.; Fayçal Hamou, R.; Ulrich Biedermann, P.; Schweinberger, F. F.; Kunz, S.; Schloegl, K.; Wiberg, G. K. H.; Ashton, S.; Heiz, U.; Mayrhofer, K. J. J.; Arenz, M. *Nature Mater.* **2013,** *12*, 919-924.

(34) Stamenkovic, V.; Mun, B. S.; Mayrhofer, K. J. J.; Ross, P. N.; Markovic, N. M.; Rossmeisl, J.; Greeley, J.; Norskov, J. K. *Angew. Chem. Int. Ed.* **2006,** *45*, 2897-2901.

(35) Escudero-Escribano, M.; Malacrida, P.; Hansen, M. H.; Vej-Hansen, U. G.; Velázquez-Palenzuela, A.; Tripkovic, V.; Schiøtz, J.; Rossmeisl, J.; Stephens, I. E. L.; Chorkendorff, I. *Science* **2016,** *352*, 73-76.

(36) Oh, A.; Baik, H.; Choi, D. S.; Cheon, J. Y.; Kim, B.; Kim, H.; Kwon, S. J.; Joo, S. H.; Jung, Y.; Lee, K. *ACS Nano* **2015,** *9*, 2856-2867.

(37) Huang, X.; Zhao, Z.; Cao, L.; Chen, Y.; Zhu, E.; Lin, Z.; Li, M.; Yan, A.; Zettl, A.; Wang, Y. M.; Duan, X.; Mueller, T.; Huang, Y. *Science* **2015,** *348*, 1230-1234.

(38) Zhang, L.; Roling, L. T.; Wang, X.; Vara, M.; Chi, M.; Liu, J.; Choi, S.-I.; Park, J.; Herron, J. A.; Xie, Z.; Mavrikakis, M.; Xia, Y. *Science* **2015,** *349*, 412-416.

(39) Niu, Z.; Becknell, N.; Yu, Y.; Kim, D.; Chen, C.; Kornienko, N.; Somorjai, G. A.; Yang, P. *Nature Mater.* **2016,** *15*, 1188-1194.

(40) Niu, G.; Zhou, M.; Yang, X.; Park, J.; Lu, N.; Wang, J.; Kim, M. J.; Wang, L.; Xia, Y. *Nano Lett.* **2016,** *16*, 3850-3857.

(41) Chen, C.; Kang, Y.; Huo, Z.; Zhu, Z.; Huang, W.; Xin, H. L.; Snyder, J. D.; Li, D.; Herron, J. A.; Mavrikakis, M.; Chi, M.; More, K. L.; Li, Y.; Markovic, N. M.; Somorjai, G. A.; Yang, P.; Stamenkovic, V. R. *Science* **2014,** *343*, 1339-1343.

(42) Hernandez-Fernandez, P.; Masini, F.; McCarthy, D. N.; Strebel, C. E.; Friebel, D.; Deiana, D.; Malacrida, P.; Nierhoff, A.; Bodin, A.; Wise, A. M.; Nielsen, J. H.; Hansen, T. W.; Nilsson, A.; StephensIfan, E. L.; Chorkendorff, I. *Nature Chem.* **2014,** *6*, 732-738.

(43) Bu, L.; Zhang, N.; Guo, S.; Zhang, X.; Li, J.; Yao, J.; Wu, T.; Lu, G.; Ma, J.-Y.; Su, D.; Huang, X. *Science* **2016,** *354*, 1410-1414.

(44) Mistry, H.; Varela, A. S.; Kühl, S.; Strasser, P.; Cuenya, B. R. *Nature Reviews Materials* **2016**, *1*, 16009.

(45) Cui, C.; Gan, L.; Heggen, M.; Rudi, S.; Strasser, P. *Nature Mater.* **2013,** *12*, 765-771.

(46) Choi, S.-I.; Xie, S.; Shao, M.; Odell, J. H.; Lu, N.; Peng, H.-C.; Protsailo, L.; Guerrero, S.; Park, J.; Xia, X.; Wang, J.; Kim, M. J.; Xia, Y. *Nano Lett.* **2013,** *13*, 3420-3425.

(47) Greeley, J.; Stephens, I. E. L.; Bondarenko, A. S.; Johansson, T. P.; Hansen, H. A.; Jaramillo, T. F.; Rossmeisl, J.; Chorkendorff, I.; Norskov, J. K. *Nature Chem.* **2009,** *1*, 552-556.

(48) Iwasawa, Y.; Asakura, K.; Tada, M. *XAFS Techniques for Catalysts, Nanomaterials and Surfaces*, Springer, New York, 2016.
(49) Sekizawa, O.; Uruga, T.; Tada, M.; Nitta, K.; Kato, K.; Tanida, H.; Takeshita, K.; Takahashi, S.; Sano, M.; Aoyagi, H.; Watanabe, A.; Nariyama, N.; Ohashi, H.; Yumoto, H.; Koyama, T.; Senba, Y.; Takeuchi, T.; Furukawa, Y.; Ohata, T.; Matsushita, T.; Ishizawa, Y.; Kudo, T.; Kimura, H.; Yamazaki, H.; Tanaka, T.; Bizen, T.; Seike, T.; Goto, S.; Ohno, H.; Takata, M.; Kitamura, H.; Ishikawa, T.; Yokoyama, T.; Iwasawa, Y. *J. Phys., Conf. Ser.* **2013**, *430*, 012020-1-4.
(50) Tada, M.; Murata, S.; Asakoka, T.; Hiroshima, K.; Okumura, K.; Tanida, H.; Uruga, T.; Nakanishi, H.; Matsumoto, S.; Inada, Y.; Nomura, M.; Iwasawa, Y. *Angew. Chem. Int. Ed.* **2007**, *46*, 4310-4315.
(51) Ishiguro, N.; Saida, T.; Uruga, T.; Nagamatsu, S.; Sekizawa, O.; Nitta, K.; Yamamoto, T.; Ohkoshi, S.; Iwasawa, Y.; Yokoyama, T.; Tada, M. *ACS Catal.* **2012**, *2*, 1319-1330.
(52) Nagamatsu, S.; Takao, S.; Samjeské, G.; Nagasawa, K.; Sekizawa, O.: Kaneko, T.; Higashi, K.; Uruga, T.; Gayen, S.; Velaga, S.; Saniyal, M. K.; Iwasawa, Y. *Surf. Sci.* **2016**, *648*, 100-113.
(53) Newville, M.; Ravel, B.; Haskel, D.; Rehr, J. J.; Stern, E. A.; Yacoby, Y. *Physica B* **1995,** *208*, 154-156.
(54) Ravel, B.; Newville, M. J. Synchrotron Radiat. **2005**, *12*, 537-541.
(55) Ankudinov, A. L.; Ravel, B.; Rehr, J. J.; Conradson, S. D. Phys. Rev. B **1998**, *58*, 7565-7576.
(56) Takao, S.; Sekizawa, O.; Nagamatsu, S.; Kaneko, T.; Yamamoto, T.; Samjeské, G.; Higashi, K.; Nagasawa, K.; Tsuji, T.; Suzuki, M.; Kawamura, N.; Mizumaki, M.; Uruga, T.; Iwasawa, Y. *Angew. Chem. Int. Ed.* **2014**, *53*, 14110-14114.
(57) Cui, C.; Gan, L.; Neumann, M.; Heggen, M.; Roldan Cuenya, B.; Strasser, P. *J. Am. Chem. Soc.* **2014**, *136*, 4813-4816.
(58) Zhang, G.; Zhao, D.; Feng, Y.; Zhang, B.; Su, D.; Liu, G.; Xu, Q. *ACS Nano* **2012**, *6*, 2226–2236.
(59) Hammer, B.; Nørskov, J. K. *Adv. Catal*. **2000**, *45*, 71-129.
(60) Markovic, N. M.; Hammer, B.; Norskov, J. K. *Phys. Rev. Lett.* **1998**, *81*, 2819-2822.
(61) Stephens, I. E. L.; Bondarenko, A. S.; Gronbjerg, U.; Rossmeisl, J.; Chorkendorff, I. *Energy Environ. Sci.* **2012**, *5*, 6744-6762.
(62) Calle-Vallejo, F.; Loffreda, D.; KoperMarc, T. M.; Sautet, P. *Nat. Chem.* **2015,** *7*, 403-410.
(63) Calle-Vallejo, F.; Martínez, J. I.; García-Lastra, J. M.; Sautet, P.; Loffreda, D. *Angew. Chem. Int. Ed.* **2014**, *53*, 1-5.

(64) Calle-Vallejo, F.; Pohl, M. D.; Reinisch, D.; Loffreda, D.; Sautet, P.; Bandarenka, A. S. *Chem. Sci.* **2017,** *8*, 2283-2289.

(65) Calle-Vallejo, F.; Tymoczko, J.; Colic, V.; Vu, Q. H.; Pohl, M. D.; Morgenstern, K.; Loffreda, D.; Sautet, P.; Schuhmann, W.; Bandarenka, A. S. *Science* **2015,** *350*, 185-189.

(66) Dubau, L.; Nelayah, J.; Asset, T.; Chattot, R.; Maillard, F. *ACS Catal.* **2017,** *7*, 3072-3081.

(67) Dubau, L.; Nelayah, J.; Moldovan, S.; Ersen, O.; Bordet, P.; Drnec, J.; Asset, T.; Chattot, R.; Maillard, F. *ACS Catal.* **2016,** *6*, 4673-4684.

(68) Chattot, R.; Asset, T.; Bordet, P.; Drnec, J.; Dubau, L.; Maillard, F. *ACS Catal.* **2017,** *7*, 398-408.

(69) Baldizzone, C.; Mezzavilla, S.; Carvalho, H. W. P.; Meier, J. C.; Schuppert, A. K.; Heggen, M.; Galeano, C.; Grunwaldt, J.-D.; Schüth, F.; Mayrhofer, K. J. J. *Angew. Chem. Int. Ed.* **2014**, *53*, 14250–14254.

Insert Table of Contents Graphic and Synopsis Here

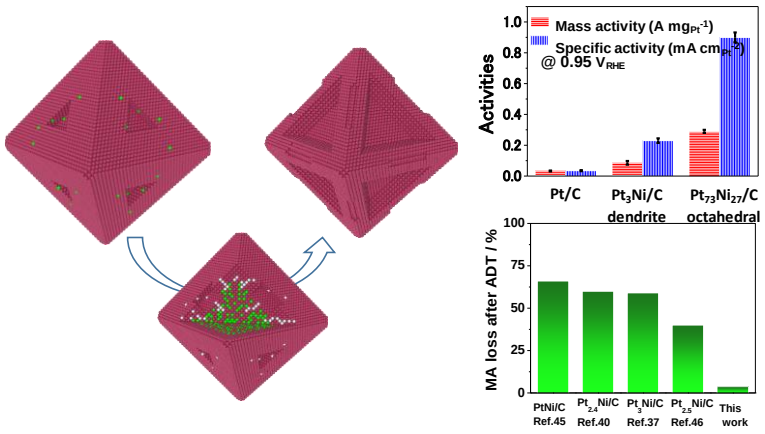

Supporting Information

Simultaneous Improvements of Performance and Durability of An Octahedral PtNix/C Electrocatalyst for Next–Generation Fuel Cells by Continuous, Compressive and Concave Pt Skin Layers

Xiao Zhao,[†] Shinobu Takao [†] Kotorao Higashi,[†] Takuma Kaneko,[†] Gabor Samjeskè,[†] Oki Sekizawa,[†] Tomohiro Sakata,[†] Yusuke Yoshida,[†] Tomoya Uruga[†,‡] and Yasuhiro Iwasawa[†]*

[†] Innovation Research Center for Fuel Cells, The University of Electro-Communications, Chofugaoka, Chofu, Tokyo 182-8585, Japan

[‡]Japan Synchrotron Radiation Research Institute, SPring-8, Sayo, Hyogo 679-5198, Japan

*Corresponding author: iwasawa@pc.uec.ac.jp

Previous synthesis methods for octahedral PtNix/C for comparison with our study

The previous synthesis methods are briefly described below. Pt alloy octahedral nnaoparticles with three initial bulk compositions $Pt_{1.5}Ni$, PtNi and $PtNi_{1.5}$ were synthesized by a one-step, surfactant-free solvothermal method, dissolving $Pt(acac)_2$ and $Ni(acac)_2$ into DMF and heating at 120 ^oC for 42 h in sealed autoclave to form concave octahedral nanostructures.[1]

In a typical synthesis of 9 nm octahedral $Pt_{2.5}Ni$ nanoparticles, $Pt(acac)_2$ and $Ni(acac)_2$ were mixed with oleylamine and oleic acid in benzyl ether, followed by the addition of $W(CO)_6$ as a source of CO at 130 ^oC in Ar and heating at 230 ^oC for 40 min.[2]

Pt@Ni/C-Pt skin nanoparticles with an octahedral skeletal structure was fabricated by treating $Pt(acac)_2$ and $Ni(acac)_2$ in stearic acid and octadecylamine under CO at 170 ^oC, followed by the second step for Pt overlayer using K_2PtCl_4 in an acetic acid/ethylene glycol solution at 90 ^oC for 5 h under Ar.[3]

Octahedral Pt_3Ni/C catalyst was also synthesized by using $Pt(acac)_2$ and $Ni(acac)_2$, benzoic acid, carbon black (Vulcan XC72R) in DMF at 160 ^oC for 12 h.[4]

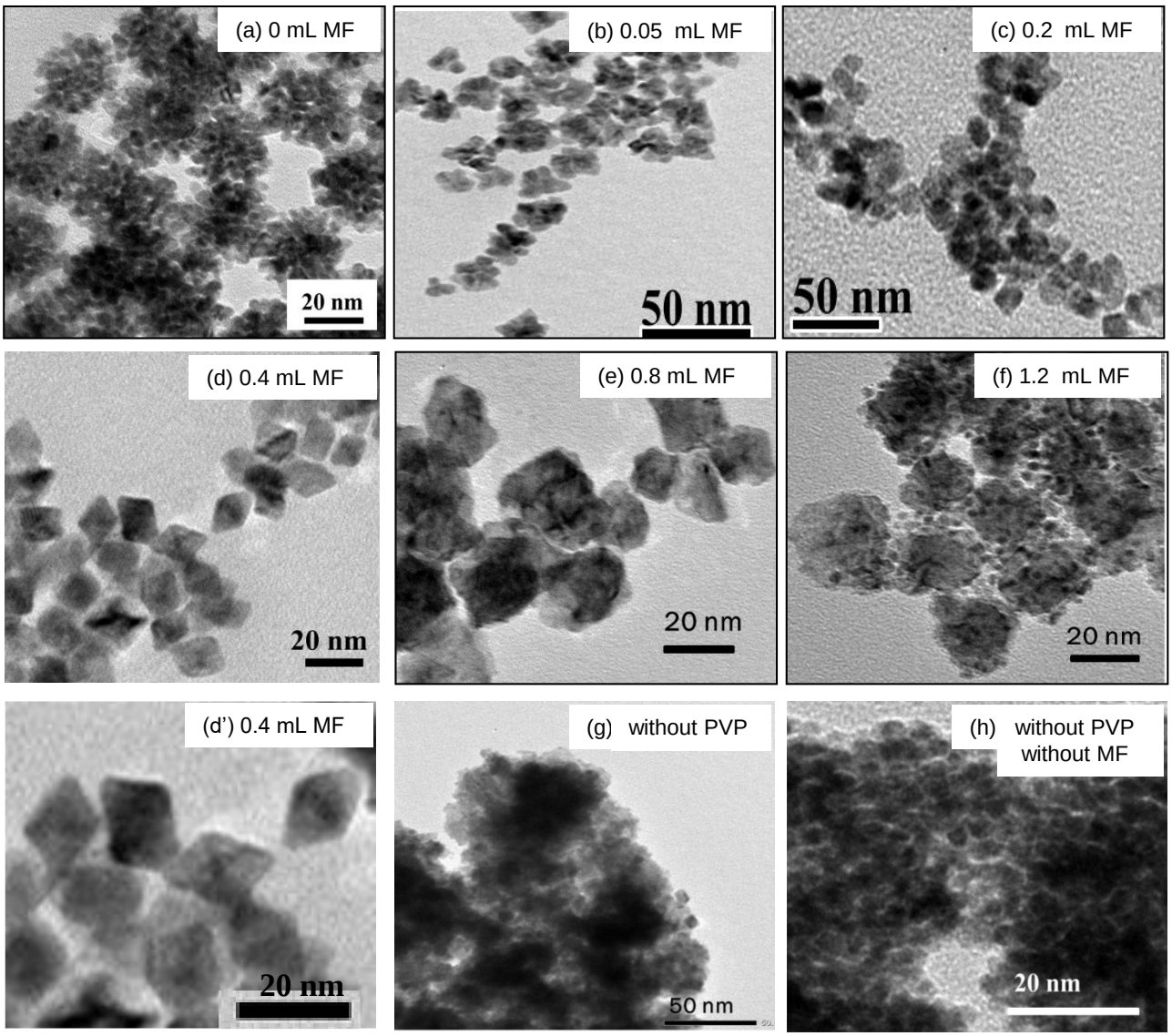

Figure S1. TEM images of various as-synthesized $PtNi_x$ nanoparticles obtained by changing the MF quantity with and without PVP. (a): PVP, (b)-(f): PVP+MF, (g): MF, (h): neither PVP nor MF.

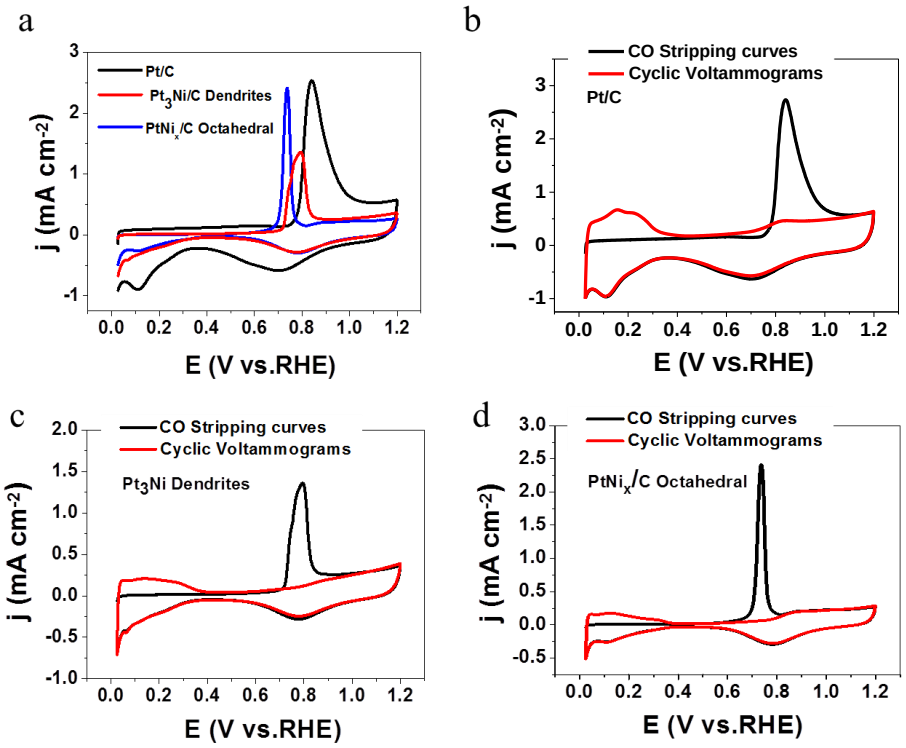

Figure S2. CO stripping curves and CVs of the catalysts: (a) The comparison of the CO stripping curves of the activated Pt/C, dendrite $PtNi_x$/C and octahedral $PtNi_x$/C; (b)-(d): the CO stripping curves and CVs of the activated Pt/C, dendrite Pt_3Ni/C and octahedral $PtNi_x$/C, respectively.

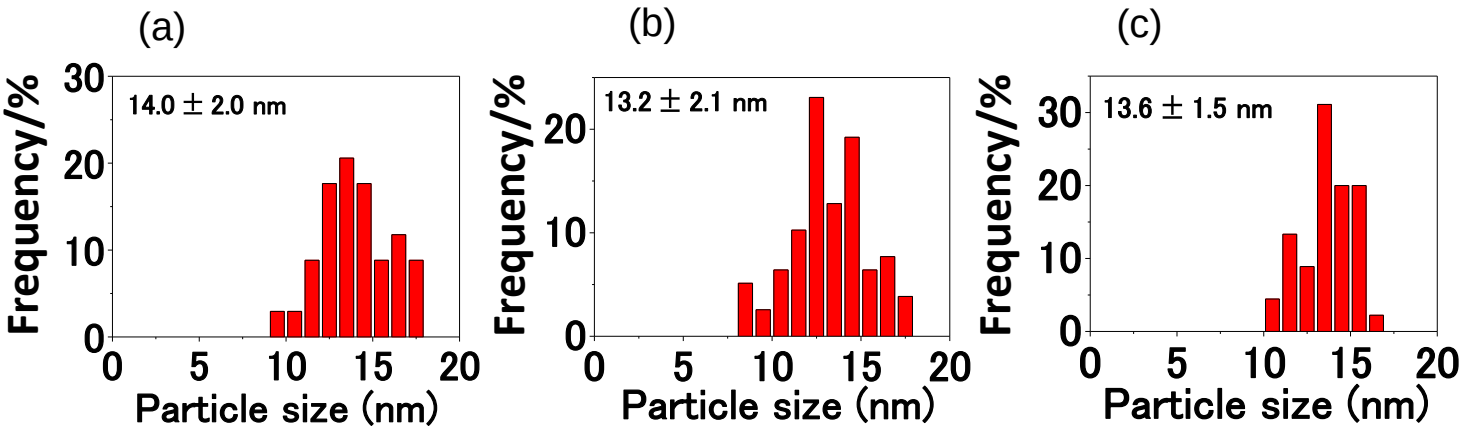

Figure S3. Histograms of particle size distribution in as-synthesized (a), activated (b) and ADT (c) $PtNi_x/C$.

(a)

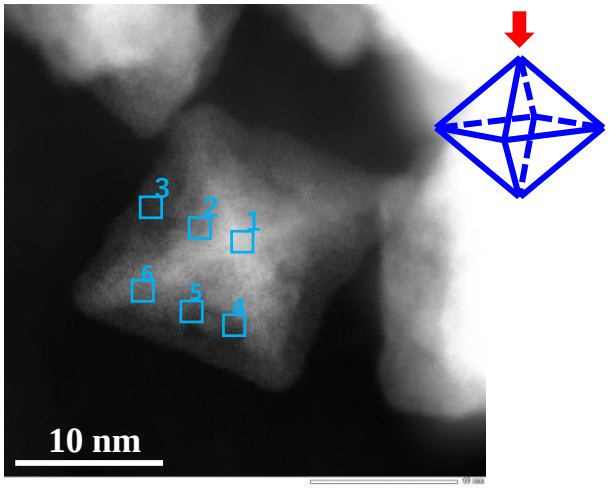

(b)

place	Pt (atomic%)	Ni (atomic%)
1	49.6	50.4
2	42.8	57.2
3	58.3	41.7
4	49.5	50.5
5	42.8	57.2
6	58.2	41.8
Total	50.2%	49.8%

(c)

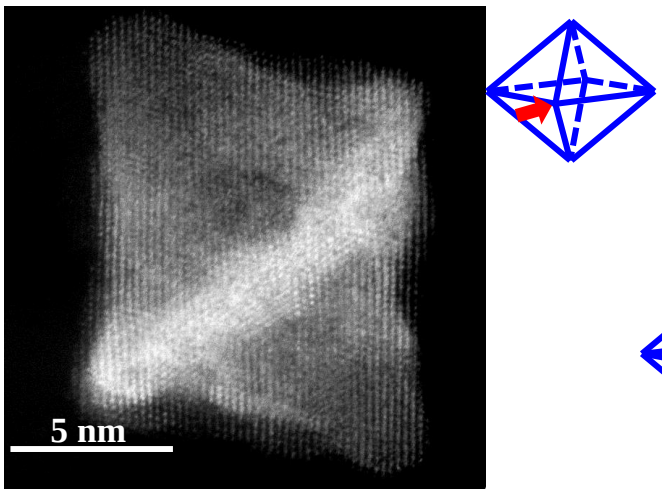

(d)

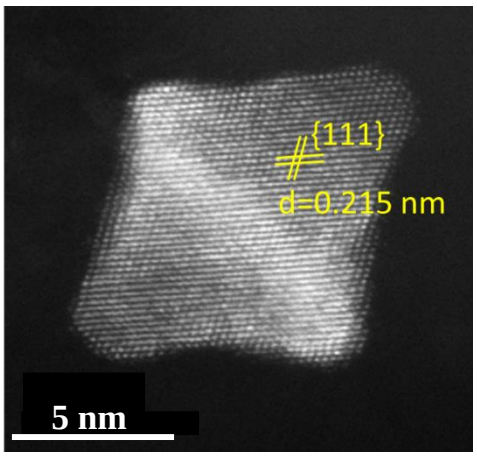

Figure S4. (a), (c), and (d) STEM images in a high angle annular dark (HAAD) field mode for as-synthesized single nanoparticles measured from the direction of the red arrows. (b) EDS area analysis for the composition of Pt and Ni at the areas 1-6 in (a) and the total amounts of Pt and Ni atoms.

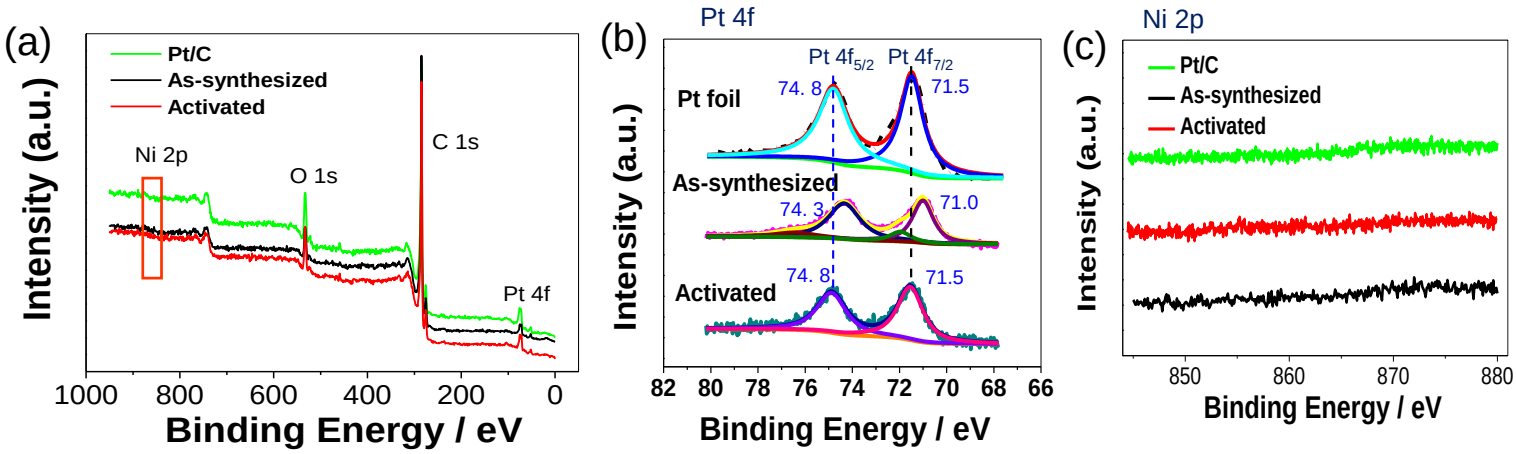

Figure S5. (a) wide scan XPS spectra, (b) XPS Pt 4f spectra, and (c) XPS Ni 2p spectra for as-synthesized (octahedral $Pt_{50}Ni_{50}$/C), activated (octahedral $Pt_{73}Ni_{27}$/C), and as-purchased Pt/C (TEC10E20E) or Pt foil.

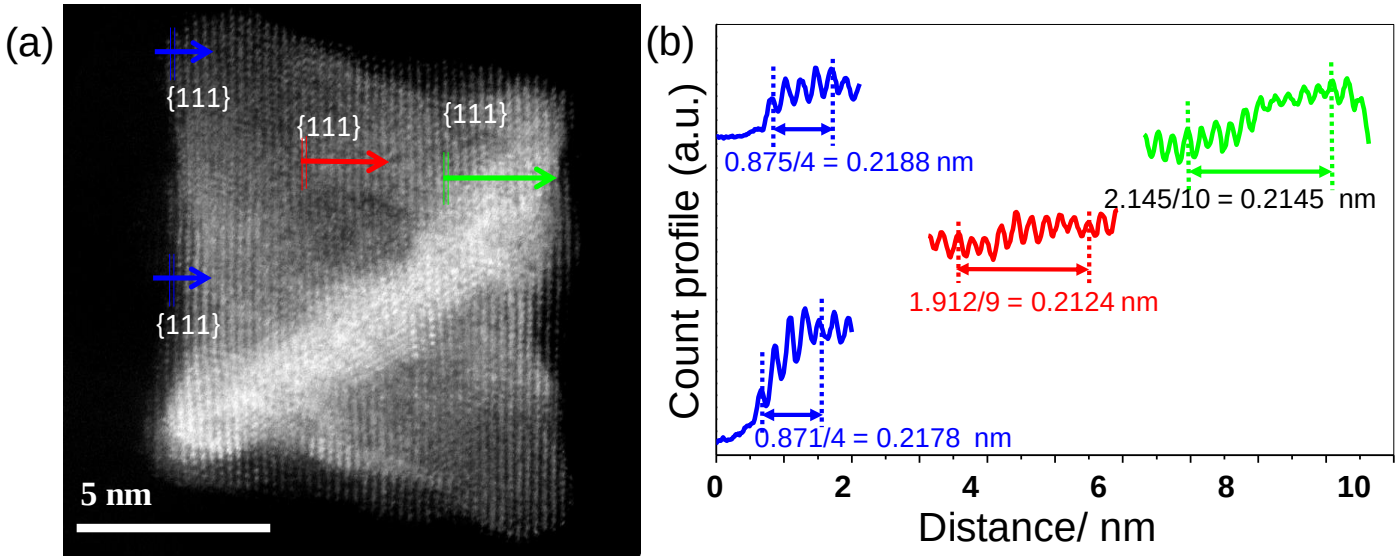

Figure S6. Compressive strain of the as-synthesized octahedral PtNi/C estimated by the atomic-scale topographic STEM-EDS analysis for the interplane spacing. (a): HAADF STEM images. (b): atomic-scale topographical analysis along each arrow in (a), respectively. (b): d(111) spacing.

The d(111) spacings near the edge were 0.2178–0.2188 nm (Figure S6), which are 3.4–3.8% compressive compared to that of Pt bulk (0.2265 nm). A place near the {111} facet center (0.2124 nm) showed 6.2% compression. The d(111) spacing near the vertex was 0.2145 nm, indicating 5.3% compression similar to the case of the d(200) spacing near the vertex.

Table S1. Compressive strains at edges, vertexes and facets in the as-synthesized $Pt_{50}Ni_{50}$/C, activated $Pt_{73}Ni_{27}$/C and ADT $Pt_{74}Ni_{26}$/C samples.

	as-synthesized $Pt_{50}Ni_{50}$/C	activated $Pt_{73}Ni_{27}$/C	ADT $Pt_{74}Ni_{26}$/C
d(200) spacing	%	%	%
Side edge	3.5	2.4	2.5-2.9
diagonal edge	-	2.8	3.2
vertex	5.6	3.6	3.2-3.6
{111} facet	7.3	1.9	2.3
d(111) spacing	%	%	%
side edge	3.4–3.8	2.2–3.0	1.5–2.5
diagonal edge	-	-	-
vertex	5.3	3.6	2.9-4.1
{111} facet	6.2	2.1	1.9

Error range: ±1%

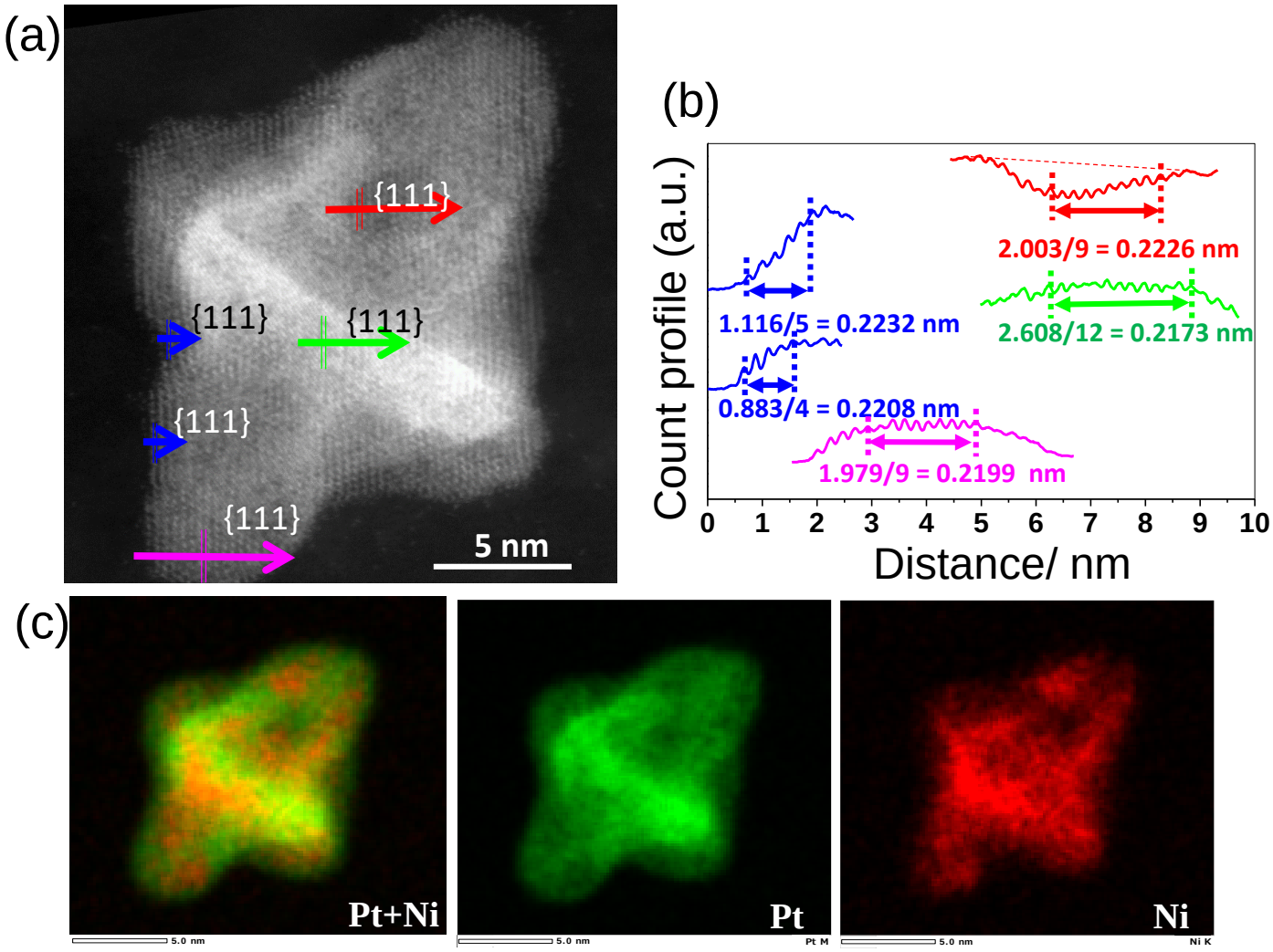

Figure S7. HAADF STEM images, atomic-scale topographic STEM-EDS line analysis, and EDS element maps for the ADT(10,000 cycles) octahedral $Pt_{74}Ni_{26}$/C. (a): STEM image, (b): Compressive strain of the ADT(10,000 cycles) octahedral $PtNi_x$/C estimated by the atomic-scale topographic STEM-EDS analysis for d(111) spacing, (c): Pt and Ni EDS maps of the same PtNi nanoparticle as (a) (scale bars: 5 nm).

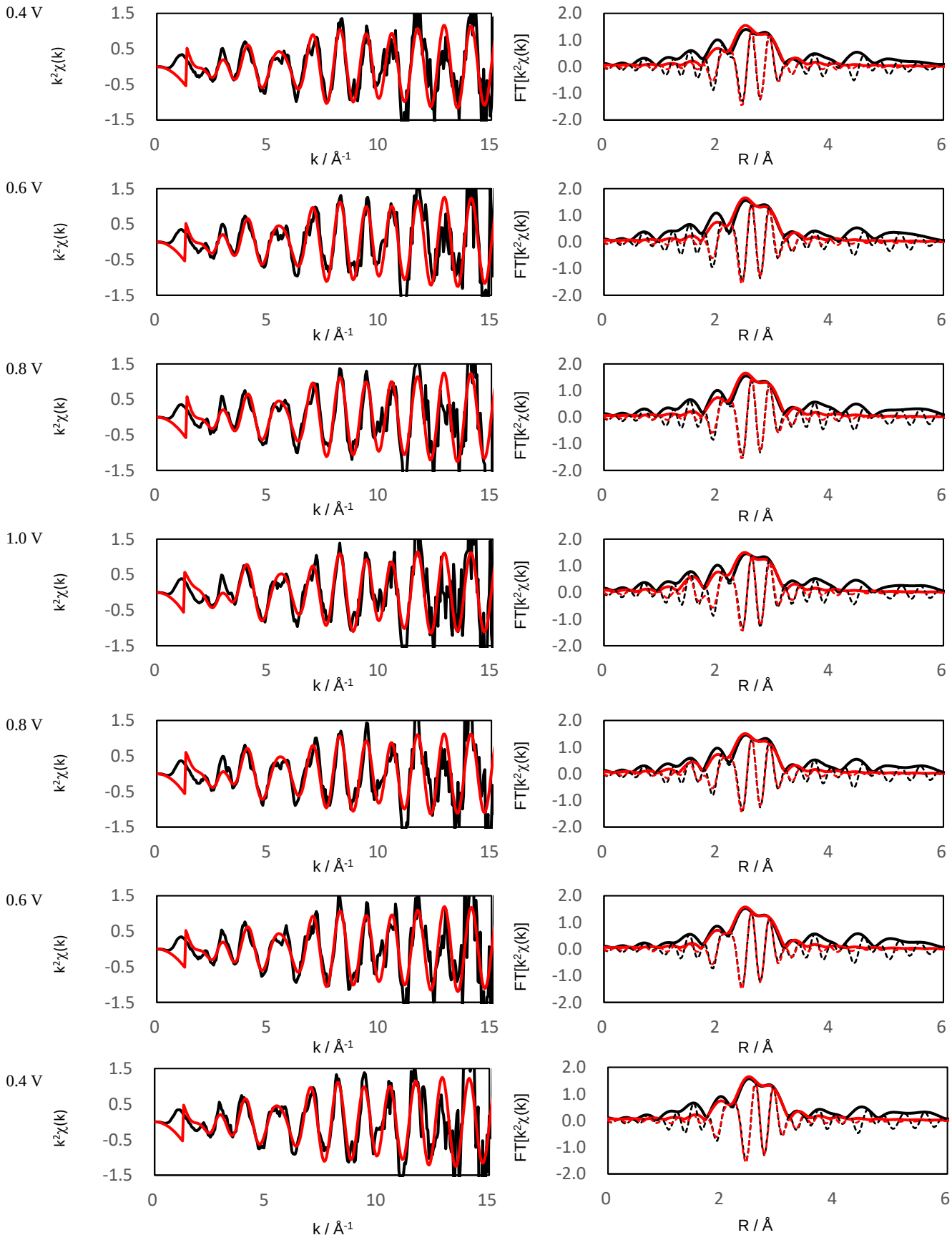

Figure S8. k^2-weighted Pt L_{III}-edge EXAFS oscillations (left) and their associated Fourier transforms (right) for activated Pt/C (TEC10E50E-HT) at 0.4 - 1.4 V_{RHE}. Fitting curves: red; Fitting ranges: 3 – 12 $Å^{-1}$ for Δk and 1.4 – 3.0 Å for ΔR.

Table S2. EXAFS analysis for activated Pt/C (TEC10E50E-HT) at 0.4-1.0 V_{RHE}.

TEC10E50E-HT	CN	(e. s. d.)	DW	ΔE_0	(e. s. d.)	R	(e. s. d.)	R-factor
Pt-Pt @ 0.4 V	10.29	1.42	0.004	6.73	3.20	2.76	0.02	0.07688
Pt-Pt @ 0.6 V	11.05	1.96	0.004	6.21	3.38	2.76	0.02	0.08356
Pt-Pt @ 0.8 V	11.03	1.26	0.004	6.79	2.85	2.76	0.01	0.05773
Pt-Pt @ 1.0 V	10.19	1.58	0.004	5.73	3.58	2.76	0.02	0.06706
Pt-O @ 1.0 V	0.77	0.60	0.001			1.95	0.06	
Pt-Pt @ 0.8 V	10.16	1.23	0.004	6.42	2.91	2.76	0.01	0.04545
Pt-O @ 0.8 V	0.48	0.47	0.001			1.96	0.07	
Pt-Pt @ 0.6 V	10.51	0.73	0.004	6.31	2.16	2.76	0.01	0.03242
Pt-Pt @ 0.4 V	11.00	1.02	0.004	6.01	2.60	2.76	0.01	0.04225

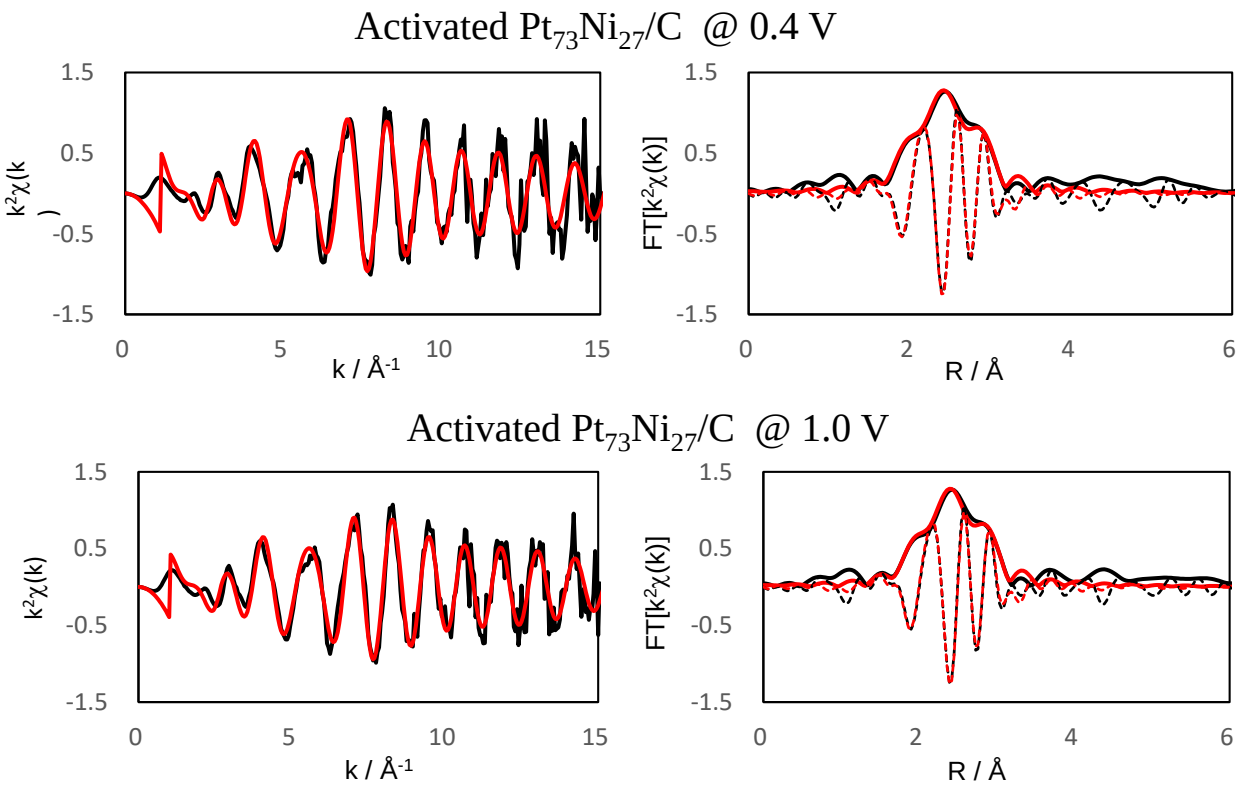

Figure S9. k^2-weighted Pt L_{III}-edge EXAFS oscillations (left) and their associated Fourier transforms (right) for activated $Pt_{73}Ni_{27}/C$ at 0.4 V_{RHE} and 1.4 V_{RHE}. Fitting curves: red; Fitting ranges: 3 – 12 $Å^{-1}$ for Δk and 1.4 – 3.0 Å for ΔR.

Table S3. EXAFS analysis for activated $Pt_{73}Ni_{27}$/C at 0.4 V_{RHE} and 1.0 V_{RHE}.

	CN	(e. s. d.)	DW	ΔE_0(eV)	(e. s. d.)	R(Å)	(e. s. d.)	R-factor
Pt-Pt @ 0.4 V	9.83	0.75	0.007	4.89	1.00	2.74	0.01	0.00627
Pt-Ni @ 0.4 V	1.13	0.49	0.010			2.65	0.03	
Pt-Pt @ 1.0 V	9.77	0.68	0.007	4.13	0.92	2.73	0.01	0.00536
Pt-Ni @ 1.0 V	1.03	0.46	0.010			2.65	0.03	

References

(1) Cui, C.; Gan, L.; Heggen, M.; Rudi, S.; Strasser, P. *Nature Mater.* **2013,** *12*, 765-771.
(2) Choi, S.-I.; Xie, S.; Shao, M.; Odell, J. H.; Lu, N.; Peng, H.-C.; Protsailo, L.; Guerrero, S.; Park, J.; Xia, X.; Wang, J.; Kim, M. J.; Xia, Y. *Nano Lett.* **2013,** *13*, 3420-3425.
(3) Oh, A.; Baik, H.; Choi, D. S.; Cheon, J. Y.; Kim, B.; Kim, H.; Kwon, S. J.; Joo, S. H.; Jung, Y.; Lee, K. *ACS Nano* **2015,** *9*, 2856-2867.
(4) Huang, X.; Zhao, Z.; Cao, L.; Chen, Y.; Zhu, E.; Lin, Z.; Li, M.; Yan, A.; Zettl, A.; Wang, Y. M.; Duan, X.; Mueller, T.; Huang, Y. *Science* **2015,** *348*, 1230-1234.